

DIFFERENTIAL RESPONSES TO
NEUROMODULATION IN MODEL NEURONS OF
THE CRUSTACEAN STOMATOGASTRIC GLAND

ALEC J HOYLAND

DIFFERENTIAL RESPONSES TO
NEUROMODULATION IN MODEL NEURONS
OF THE CRUSTACEAN STOMATOGASTRIC
GANGLION

Master's Thesis
Presented to
The Faculty of the Graduate School of Arts and Sciences
Brandeis University
Interdisciplinary Program in Neuroscience
Eve Marder, Advisor
In Partial Fulfillment
of the Requirements for the Degree
Master of Science
in
Neuroscience
by
Alec J Hoyland

May 2018

This program is free software: you can redistribute it and/or modify it under the terms of the GNU General Public License as published by the Free Software Foundation, either version 3 of the License, or (at your option) any later version.

See <http://www.gnu.org/licenses/>.

Copyright by
Alec J Hoyland
© 2018

The greatest enemy of knowledge is not ignorance, it is the illusion
of knowledge.

– Stephen Hawking (1942-2018)

ABSTRACT

Neuronal networks must produce stable circuit output for sustained periods of time despite environmental perturbation. In addition, they must be sensitive to key endogenous signaling to produce differing output. The [STG](#) manages these competing objectives while remaining degenerate to ion channel density. Neuromodulators can produce a diverse set of network states using the same cellular and synaptic morphology. In particular to the [STG](#), the dense, tangled neuropil and gradations in reversal potential render neurons isopotential with respect to the somata. Neuromodulators, then, play the role of maintaining and switching network activity. For stable and responsive biological activity, degenerate networks must still be robust to environmental perturbation and responsive to intentional modulation. In this thesis, I describe red pigment-concentrating hormone ([RPCH](#)) acting as a neuromodulator on a computational model of a rhythmic motor circuit.

*The most exciting phrase to hear in science,
the one that heralds new discoveries,
is not 'Eureka!', but 'That's funny...'.*

ACKNOWLEDGMENTS

Thank you to everyone I have forced into a conversation about neuroscience with me, namely Aparna Baskaran, Lishibanya Mohapatra, Mara Chin-Purcell Rue, and Ekaterina Morozova. Thank you as well to Srinivas Gorur-Shandilya, without whom this thesis would not have been possible. Thank you to Jané Kondev, Eve Marder, and the Quantitative Biology Research Community for encouraging me to explore without bounds.

I also owe a great debt to my family: Jeffrey, Randi, and Sienna, and my adoptive family: Matthew, Deborah, Gwendolyn, Vanna de Graaff the keeshond, Norman the hedgehog, and Frederick and Boris the tortoises.

CONTENTS

1	INTRODUCTION	1
1.1	The Stomatogastric Ganglion	1
1.2	The Pyloric Rhythm	3
1.3	Neurodynamics	6
1.4	Modeling the Stomatogastric Ganglion	7
2	METHODS	9
2.1	Model Parameters	9
2.2	Simulating Model Neurons	11
2.3	The Prinz Database	11
2.4	Modulatory Input	12
2.5	Model Implementation	13
2.5.1	Parameter Optimization	14
2.5.2	Computing Metrics	16
2.5.3	Designing the Cost Function	17
3	RESULTS	20
3.1	Modulation in AB Models Switches Between Amplitude States	21
3.2	Variability in Network Response to Modulation	23
3.2.1	Neuromodulation Increases Frequency and Amplitude	23
3.2.2	Modulation of AB-PD and LP Promotes Robust Pyloric Rhythms	28
3.2.3	Modulation of LP Can Inhibit AB-PD	36
3.2.4	Modulation of AB Can Elicit Tonic Spiking	36
4	CONCLUSION	42
A	APPENDIX	48
A.1	Maximal Conductances for Model Neurons	48
A.2	Supplemental Figures	54
	BIBLIOGRAPHY	56

LIST OF FIGURES

Figure 1.1	The stomatogastric ganglion	2
Figure 1.2	Circuit diagram of the STG	3
Figure 1.3	Circuit diagram of the pyloric circuit	4
Figure 1.4	Pyloric Rhythms in RPCH	5
Figure 1.5	Proctolin on AB neurons	5
Figure 1.6	Network degeneracy in model pyloric circuits.	8
Figure 2.1	Voltage dependence for model currents	9
Figure 2.2	Pyloric network model architecture	12
Figure 2.3	Models of modulatory input current	13
Figure 2.4	Parameter optimization using different algorithms	16
Figure 2.5	Estimating burst metrics	17
Figure 2.6	Savitzky-Golay filter visualizes slow wave . . .	19
Figure 3.1	Three motifs of modulation in model AB neurons	21
Figure 3.2	Summary statistics of database models with modulatory input	22
Figure 3.3	Superimposed model AB traces	23
Figure 3.4	Network with modulation into AB-PD (traces)	24
Figure 3.5	Network with modulation into AB-PD (metrics)	25
Figure 3.6	Network with modulation into LP (traces) . . .	25
Figure 3.7	Network with modulation into LP (metrics) . .	26
Figure 3.8	Network with modulation into AB-PD & LP (traces)	27
Figure 3.9	Network with modulation into AB-PD & LP (metrics)	28
Figure 3.10	Cross-correlations in AB-PD model maximal conductances	29
Figure 3.11	Cross-correlations in LP model maximal conductances	30
Figure 3.12	Cross-correlations in PY model maximal conductances	31
Figure 3.13	Cross-correlations in synaptic maximal conductances	32
Figure 3.14	Distribution of rhythmicity in network models	33
Figure 3.15	All optimized ABPD models in decentralized and modulated cases	34
Figure 3.16	All optimized ABPD models in decentralized and modulated cases	35
Figure 3.17	All optimized ABPD models in decentralized and modulated cases	35
Figure 3.18	Modulation onto LP inhibits the pacemaker (traces)	38

Figure 3.19	Modulation onto LP inhibits the pacemaker (metrics)	38
Figure 3.20	Modulation onto LP does not increase frequency (traces)	39
Figure 3.21	Modulation onto LP does not increase frequency (metrics)	39
Figure 3.22	Modulation of AB-PD depolarizes AB-PD (traces)	40
Figure 3.23	Modulation of AB-PD depolarizes AB-PD (metrics)	40
Figure 3.24	Modulation of AB-PD can elicit tonic spiking (traces)	41
Figure 3.25	Modulation of AB-PD can elicit tonic spiking (metrics)	41
Figure 4.1	Burst frequency dose response to oxotremorine	43
Figure 4.2	Long timescale oscillations in RPCH and TTX	45
Figure 4.3	RPCH and TTX in optimized AB-PD models .	46
Figure A.1	Database models with modulatory input	54
Figure A.2	Responsive database models with modulatory input	54
Figure A.3	Optimized database models increase in frequency and amplitude	55
Figure A.4	Optimized database models smoothly increase in frequency and amplitude	55

LIST OF TABLES

Table 2.1	Reversal potentials for model currents	10
Table 2.2	Constants for model synapses	11
Table 2.3	Initial conditions	11
Table 2.4	Modulatory input current models	13
Table 2.5	Pyloric network metric bounds	18
Table 2.6	Pyloric network metric ratios	19
Table 3.1	Correlation between pyloric activity in different modulation states	34
Table A.1	Maximal conductances for Figure 3.3.	48
Table A.2	Maximal conductances for Figure 3.4.	48
Table A.3	Maximal conductances for Figure 3.4.	49
Table A.4	Maximal conductances for Figure 3.6.	49
Table A.5	Maximal conductances for Figure 3.6.	49
Table A.6	Maximal conductances for Figure 3.8.	50
Table A.7	Maximal conductances for Figure 3.8.	50
Table A.8	Maximal conductances for Figure 3.18.	50
Table A.9	Maximal conductances for Figure 3.18.	51

Table A.10	Maximal conductances for Figure 3.20	51
Table A.11	Maximal conductances for Figure 3.20	51
Table A.12	Maximal conductances for Figure 3.22	52
Table A.13	Maximal conductances for Figure 3.22	52
Table A.14	Maximal conductances for Figure 3.24	52
Table A.15	Maximal conductances for Figure 3.24	53

LISTINGS

ACRONYMS

AB	anterior burster cell
CCAP	crustacean cardioactive peptide
CoG	commissural ganglion
CPG	central pattern generator
IC	inferior cardiac cell
I_{Na}	fast sodium current
I_{CaT}	fast transient calcium current
I_{CaS}	slow calcium current
I_A	fast transient potassium current
I_{KCa}	calcium-dependent potassium current
I_{Kd}	delayed rectifier potassium current
I_H	hyperpolarization-activated mixed-cation inward current
I_{leak}	passive ion leak current
I_{MI}	modulatory input current
I_{glut}	glutamatergic synaptic current
I_{chol}	cholinergic synaptic current
LP	lateral pyloric cell

OG	oesophageal ganglion
PD	pyloric dilator cell
PY	pyloric cell
RPCH	red pigment-concentrating hormone
STG	stomatogastric ganglion
STNS	stomatogastric nervous system
TTX	tetrodotoxin
VD	ventricular dilator cell

INTRODUCTION

Any rhythmic motor behavior necessary to life must be stable under environmental perturbation, yet sensitive to internal cues from the organism. Respiration, for instance, must continue interminably, but must also be able to account for the holding of one's breath against noxious stimuli or increase in amplitude or frequency during exercise.

Many rhythmic behaviors begin as activity in central pattern generators (**CPGs**), neuronal circuits which intrinsically produce rhythmic motor patterns in the absence of sensory or descending inputs¹. A central pattern generator must be robust to environmental perturbation to avoid losing rhythmicity. Simultaneously, it must be responsive to intended modulation from within the organism. In respiration, for instance, serotonin neuromodulation maintains **CPG** activity in respiration; disruption of neuromodulation can result in hypoxia or death^{2,3}. The interplay between stability and sensitivity permit the same circuit to produce multiple outputs as a response to endogenous modulation⁴.

Neuronal circuits which are not tightly tuned are degenerate; there are many solutions, viable sets of parameters, which produce similar network output⁵⁻⁸. For stable and responsive biological activity, degenerate networks must still be robust to environmental perturbation and responsive to intentional modulation. In this thesis, I describe red pigment-concentrating hormone (**RPCH**) acting as a neuromodulator on a computational model of a rhythmic motor circuit.

1.1 THE STOMATOGASTRIC GANGLION

The stomatogastric nervous system (**STNS**) provides an excellent model system for analyzing how circuit dynamics arise from neuronal properties and network connectivity⁹. Initial work began in the 1970s using the **STNS** to understand central pattern generation¹⁰⁻¹². Several properties make this system ideal for electrophysiological and computational analysis.

The **STNS** consists of a group of four linked ganglia: the paired commissural ganglia (**CoG**), the oesophageal ganglion (**OG**), and the stomatogastric ganglion (**STG**)^{13,14}. Each of the **CoGs** contains approximately 400 neurons and the **OG** contains approximately 18 neurons. The stomatogastric ganglion (**STG**) is comprised of approximately 30 neurons – the exact number varies between species and between animals. In the healthy animal and *in-vitro* preparation, the **STG** produces

a triphasic motor rhythm with a frequency of about 1 Hz^{1,15}. When pharmacologically isolated, most **STG** neurons fire tonically but can be induced to conditionally burst under the influence of neuromodulators or graded inhibitory input¹⁶.

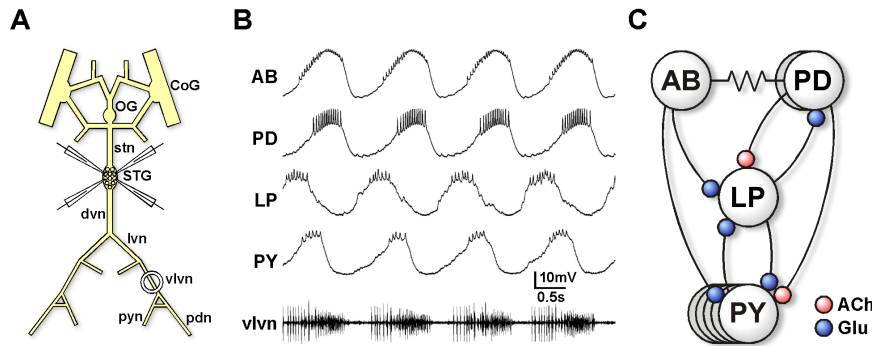


Figure 1.1: The stomatogastric ganglion. (A) Diagram of the **STNS** showing the ganglia (capitals) and the major nerves (lowercase). (B) Intracellular recordings from four cells in the pyloric circuit of the **STG**. The fifth trace shows extracellular *vlvn* nerve recording, which contains potentials from the above cells. (C) Circuit diagram showing synaptic connectivity in the pyloric circuit. Resistor symbols indicate electrical synapses. **ACh** are acetylcholinergic and **Glu** are glutamateric synapses, where balls indicate post-synaptic targets¹⁷.

STG neurons have large somata (typically 50-100 microns across) and complex dendritic morphology^{18,19}. While these cells possess long axons which contribute to descending nerves, much of the arborization consists of neurites which tangle extensively in the neuropil. This wiring follows a space-filling mechanism. Despite this tangled morphology, **STG** neurons are electronically compact. Gradients in reversal (Nernst) potential as a function of path distance from the soma maintain signal amplitude near and far from zones of integration¹⁸. Therefore, the circuit relies on intrinsic and synaptic properties instead of morphological tuning to produce network activity.

Robustness to mechanical insult permits dissection and electrophysiological recording *in-vitro*. The fictive motor patterns produced by the **STG** survive for at least 24 hours without incubation and are representative of both the activity of the circuit *in-vivo* and the motor output²⁰. Additionally, since most synaptic connections in the **STG** occur between motor neurons, the circuit can be isolated from descending interneurons²¹⁻²³. Decentralization by severing the *stn*, the descending nerve which connects the **CoGs** and **OG** to the **STG**, removes descending neuromodulation.

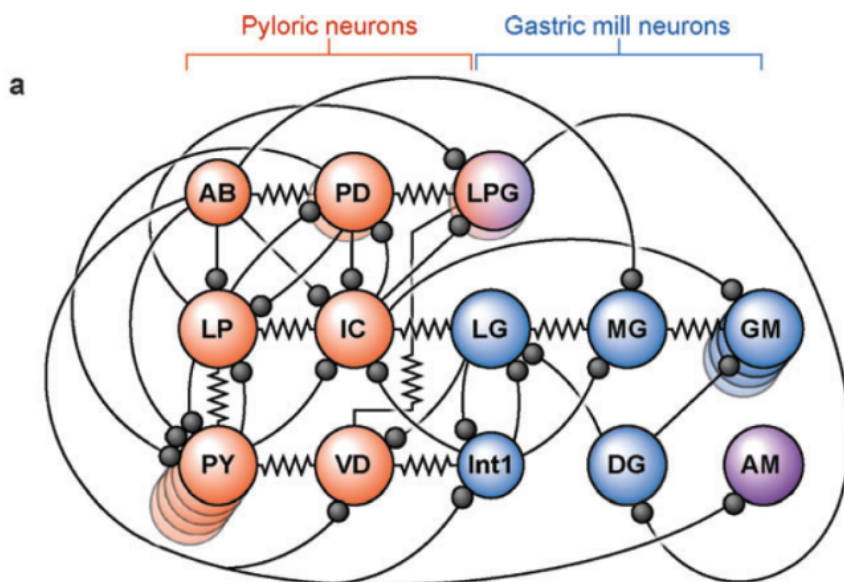


Figure 1.2: Circuit diagram of the stomatogastric ganglion (STG). Circles are neurons, resistor symbols are electrical synapses, balls indicate post-synaptic inhibitory targets.¹⁷.

1.2 THE PYLORIC RHYTHM

The pyloric rhythm is a triphasic motor pattern almost always continuously expressed in the healthy crustacean^{24,25}. The frequency of the rhythmic behavior may vary over [0.5, 2.5] Hz, but the burst order, phase relationships, and duty cycle are maintained in healthy animals²⁶. The canonical pyloric rhythm consists of bursts of action potentials in the pyloric dilator (PD) neurons, followed by bursts in the lateral pyloric (LP) neuron, and finally by bursts in the pyloric (PY) neurons. The inferior cardiac (IC) neuron fires often with the (LP) neuron and the ventricular dilator (VD) neuron fires frequently with the PY neurons¹⁴. The anterior burster (AB) interneuron projects through the stomatogastric nerve to the CoGs and is electrically coupled to the twin PD neurons.

In normal pyloric activity, the AB neuron intrinsically oscillates. The PD neurons, electrically coupled to AB, burst in phase. The AB and PD cells inhibit LP and PY, which both burst during PD interphase. LP rebounds from inhibition faster than PY and bursts first. LP and PY are in a phase-antiphase ‘half-center’ oscillator regime of mutual inhibition (Figure 1.1). PY neurons rebound and inhibit LP to terminate bursting in the coupled cell^{14,26,27}. In this regime, AB is considered the intrinsic pacemaker and AB-PD the pacemaker kernel. Selective photo-inactivation of cell types and glutamate-blocker experiments show that AB reliably maintains oscillations while decoupled¹³. The phaselocking of LP and PY during PD interphase is dependent on the intrinsic and synaptic characteristics of the network.

The pyloric rhythm is robust to perturbation. The circuit is most stable under physiological conditions (11 deg. C with descending neuromodulatory input), however the STG can maintain the phase differences characteristic of pyloric rhythmicity at temperatures up to 31 deg. C and under long-term decentralization^{20,22,23,28}.

While the pyloric rhythm is robust to environmental perturbation, it is also susceptible to neuromodulation, allowing for flexibility in network output while maintaining stability. Neuromodulators are released into the neuropil as a consequence of sensation in the animal or descending modulatory projections from the CoGs and OG^{1,4,16,29,30}.

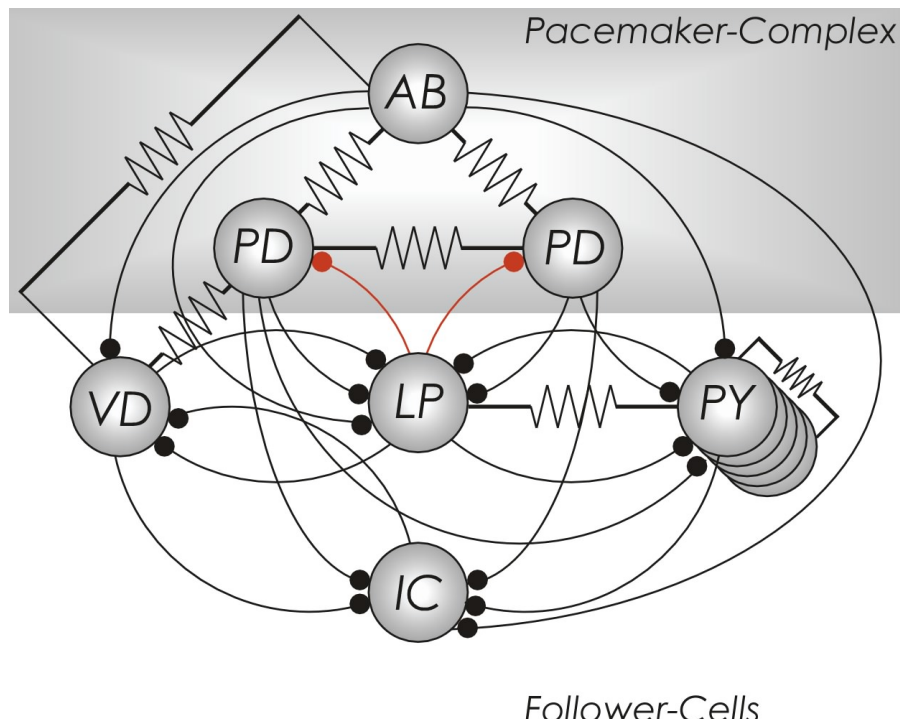


Figure 1.3: Circuit diagram of the pyloric circuit. Resistor symbols represent electrical synapses, dots represent inhibitory synapses. AB and PD form the pacemaker kernel.

The STG is multiply-modulated. The pericardial organ and other neurosecretory organs secrete neuromodulators into the neuropil which colocalize in specific neurons. In addition, many hormones circulating in the hemolymph can also act as neuromodulators in the STG^{16,17,31}.

In general, neuromodulators enhance the flexibility of neuronal networks. In one such method, neuromodulators activate a new current I_{MI} , a fast, non-inactivating, voltage-gated inward current which predominately activates between -40 mV and -20 mV^{32,33}.

All cells in the pyloric circuit are capable of activating I_{MI} through modulatory action, though they vary in its response. Differential receptor expression leads to variability and flexibility in cellular and network response to modulatory chemicals^{34,35}.

Application of red-pigment concentrating hormone (**RPCH**) to the **STG** increases the frequency and amplitude of slow-wave oscillations in the pyloric circuit, while phase relationships are maintained³⁶ (Figure 1.4, P. Rosenbaum, unpublished). Thus, the nerves which innervate the pylorus transmit the same patterned activity at the desired frequency, maintaining muscle tonus.

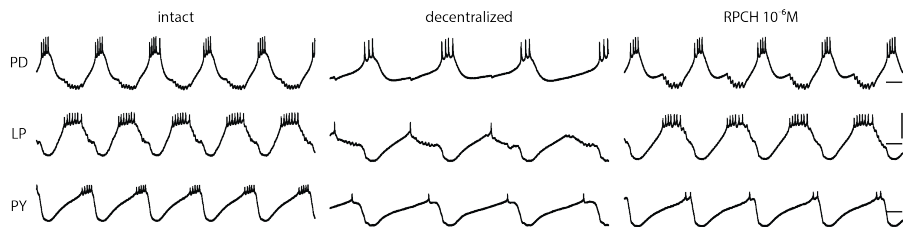


Figure 1.4: Pyloric rhythms in **RPCH**. Traces on the left show a regular pyloric rhythm in the intact **STNS**. Intracellular recordings of **PD**, **LP**, and **PY** and an extracellular recording of the *lvn* (lateral ventricular nerve) show the coordinated, triphasic rhythm. The intact rhythm has a frequency of about 1 Hz. Following decentralization (middle trace) the rhythm frequency and spikes per burst in all neurons decreased. After application of 1 μ M **RPCH**, the rhythm sped up and spikes per burst increased. Horizontal scale bars denote the membrane potential at -50 mV, vertical scale bars mark 20 mV (P. Rosenbaum, unpublished).

Three models of **I_{MI}** were examined. The first, published in Sharp *et al.*, mimics proctolin in **AB** neurons of *C. borealis* using dynamic clamp³⁷. The characteristic increase in burst frequency and slow-wave amplitude under **I_{MI}** is shown in Figure 1.5.

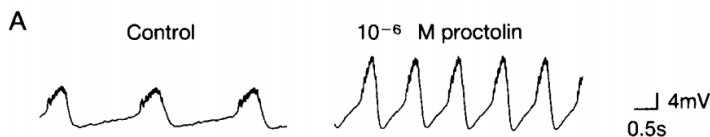


Figure 1.5: Proctolin increases amplitude and frequency of **AB** oscillations. Intracellular recording from a lobster **AB** neuron in control saline and 1 μ M proctolin.³⁷.

Swensen & Marder fit current-voltage and dosage-response curves to proctolin in **PD** and **PY** neurons^{38,39}. The **STG** was decentralized from descending neuromodulatory inputs with sucrose block and artificial proctolin current was added via dynamic clamp, based on IV curves.

Soto-Treviño *et al.* developed a model of the pacemaker kernel based on recordings in spiny lobsters⁴⁰. Neuromodulatory inputs into the **AB** neuron were modeled by **I_{MI}**. The current was fit to the model, rather than to biological data. The parameters of the current satisfied the constraints that the model would mimic decentralized behavior without the current, and control behavior with the current.

1.3 NEURODYNAMICS

Analysis of high-dimensional conductance-based models form the backbone of this thesis. Each neuron is considered to consist of compartments, each with membrane properties and a collection of ionic and synaptic currents^{41,42}. The membrane potential V_m of a compartment evolves according to the Hodgkin-Huxley formalism, which envisions excitable membranes as capacitors with variable resistors in parallel⁴³. The membrane potential evolves over time as a function of the sum of the transmembrane currents. This is described by the conservation of current equation for a capacitative membrane.

$$C_m \frac{dV_m}{dt} = - \sum_i I_i \quad (1.1)$$

where C_m is the membrane capacitance and I_i each current. Each current is described as non-Ohmic with conductance g .

$$I_i(V_m) = g_i(V_m)(V_m - E_i) \quad (1.2)$$

$$g_i(V_m) = \bar{g}_i m_i^{p_i} h_i^{q_i} \quad (1.3)$$

where

\bar{g} maximal conductance

m activation gating variable

h inactivation gating variable

p, q integer exponents

E reversal (Nernst) potential

The gating variables m and h are bounded in $[0, 1]$ so that the effective conductance $g_i(V_m)$ from the i^{th} conductance lies between zero and the maximal conductance. When $m = 0$, no channels of that conductance are open; when $h = 0$, all channels of that conductance are inactivated.

The gating variables evolve with time

$$\tau_x(V_m) \frac{dx}{dt} = x_\infty(V_m) - x \quad (1.4)$$

where

$x = (m, h)$

τ_x time constant

x_∞ steady-state function

Each conductance has characteristic steady-state and time constant functions which describe its role in the neurodynamics. The steady-states generally take the form of Boltzmann functions, fit from experiment⁴⁴.

In most models, reversal potentials for all ions excepting Ca^{2+} are fixed to constants, owing to the large ion concentration inside and

outside the cell with respect to the number of ions fluxed^{42,45}. Intracellular calcium concentration changes as a function of calcium buffering rate and calcium currents.

$$\tau_{Ca} \frac{d [Ca^{2+}]}{dt} = [Ca^{2+}]_\infty - [Ca^{2+}] \quad (1.5)$$

The steady-state function $[Ca^{2+}]_\infty (I_{Ca})$ is a function of the calcium currents; the actual calcium current lags with the time constant.

$$[Ca^{2+}]_\infty (I_{Ca}) = -f \sum_{Ca} I_{Ca} + [Ca^{2+}]_0 \quad (1.6)$$

In this context, f is a buffering coefficient which translates the calcium flux (in units of current per area) into a steady-state concentration. $[Ca^{2+}]_0$ represents the equilibrium intracellular calcium concentration.

Similarly, membrane capacitance is generally taken to be constant, following seminal work by Huxley, showing that the specific membrane capacitance varies on [9, 15] nF/mm². In models, the membrane capacitance is typically set to unity^{42,46–48}.

From the complex nonlinear interplay of several conductances, neuronal dynamics emerge.

1.4 MODELING THE STOMATOGASTRIC GANGLION

The steady-state and time constant functions are based on experimental data by⁴⁴. IV curves and current traces in voltage clamp were produced. Steady-states were fit to Boltzmann functions.

$$x_\infty(V_m) = \frac{1}{1 + \exp\left(\frac{V + V_{th}}{V_\sigma}\right)}$$

where V_{th} is the half-potential (i.e. $x_\infty(V_{th}) = 0.5$) and V_σ describes the width of the distribution. Timescales were extracted from the current traces, and generally take the form of Hill functions.

Neurons in the **STG** are isopotential. Projections in the **STG** operate on a space-filling mechanism, resulting in a dense neuropil¹⁹. Effective reversal potentials vary by path length from soma, so that **STG** neurons are electrotonically compact¹⁸. Response in the soma is comparable to elsewhere, meaning that the cells are isopotential.

Strogatz explains that, "No insight is gained if the model is as perplexing as the phenomena it is supposed to describe,"⁴⁹. To this end, conductance-based models of the **STG** have strived for verisimilitude only so much as to encompass te burst characteristics, phase relationships, and other neurocomputational properties of the circuit.

Since STG neurons are electronically compact, single-compartment (isopotential) models are suitable for representing time-correlated circuit output^{41,46,50}. In real cells, action potentials begin in the spike-initiation zone, so that spikes appear attenuated in somatic recordings. This can be rectified in computational models by creating two-compartment models, increasing realism at the expense of increasing the complexity⁴⁰.

Single-compartment conductance-based models demonstrate that diverse sets of maximal conductances can produce spiking activity. While the set of points in conductance space which elicit spiking behavior is not ergodic, the spiking subspace is much larger than initially expected⁴⁶. In three-cell networks (AB-PD, LP, PY), simulations elicited similar network activity from disparate network parameters, showing the theoretical possibility of significant network degeneracy⁴⁷. These theoretical intuitions are supported by electrophysiology and mRNA assays, which demonstrate highly variable animal-to-animal mRNA and channel expression^{34,51,52}.

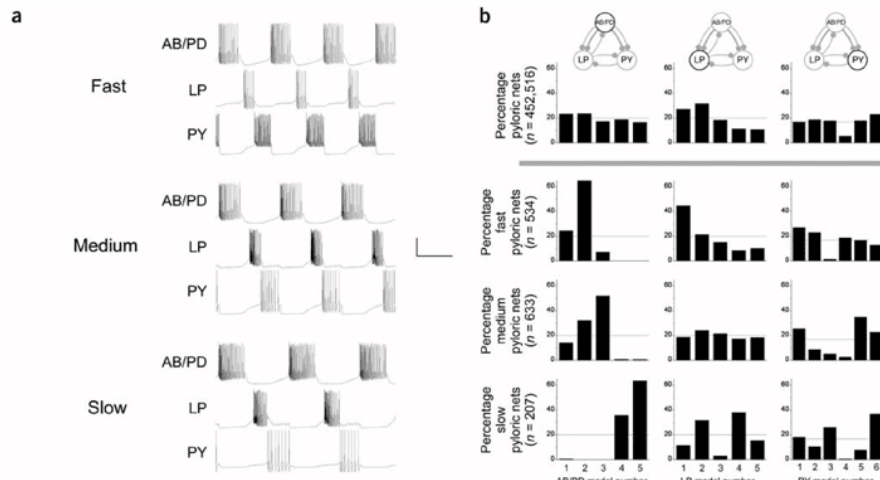


Figure 1.6: Network degeneracy in model pyloric circuits. (a) Voltage traces from simulated pyloric networks in fast, medium, and slow burst-frequency ranges. Scale bars, 1 s and 50 mV. (b) Percentages of pyloric networks that contain a given AB-PD model neuron (left), LP model neuron (middle), or PY model neuron (right). Top row, distributions for all pyloric networks; bottom rows, distributions for fast, medium and slow pyloric networks⁴⁷.

It has been demonstrated that there are many ways to produce stable, predictable output in models, as in animals, but these models have not been tested in response to modulation. Neuromodulation is a key way by which a neuronal circuit can be robust to unwelcome perturbation yet still respond with specialized activity when modulated. Network degeneracy comes secondary to this biological necessity.

2

METHODS

For much of this thesis, single-compartment model neurons with Hodgkin-Huxley type membrane currents and an intracellular calcium buffer were used^{43,53,54}. Similar models have been described previously^{42,46,47,55}. The membrane currents are based on experiments on *Homarus* neurons⁴⁴.

Briefly, the currents consist of a fast sodium current (I_{Na}), a fast transient calcium current (I_{CaT}), a slow calcium current (I_{CaS}), a fast transient potassium current (I_A), a calcium-dependent potassium current (I_{KCa}), a delayed rectifier potassium current (I_{Kd}), a hyperpolarization-activated mixed-cation inward current (I_H), and a passive ion leak current (I_{leak}).

2.1 MODEL PARAMETERS

Model parameters were adapted from^{46,47}

	p	m_∞	h_∞	τ_m	τ_h
I_{Na}	3	$\frac{1}{1 + \exp\left(\frac{V + 25.5}{-5.29}\right)}$	$\frac{1}{1 + \exp\left(\frac{V + 48.9}{5.18}\right)}$	$2.64 - \frac{2.52}{1 + \exp\left(\frac{V + 120}{-25}\right)}$	$\frac{1.34}{1 + \exp\left(\frac{V + 62.9}{-10}\right)} * \left(1.5 + \frac{1}{1 + \exp\left(\frac{V + 34.9}{3.6}\right)}\right)$
I_{CaT}	3	$\frac{1}{1 + \exp\left(\frac{V + 27.1}{-7.2}\right)}$	$\frac{1}{1 + \exp\left(\frac{V + 32.1}{5.5}\right)}$	$43.4 - \frac{42.6}{1 + \exp\left(\frac{V + 68.1}{-20.5}\right)}$	$210 - \frac{179.6}{1 + \exp\left(\frac{V + 55}{-16.9}\right)}$
I_{CaS}	3	$\frac{1}{1 + \exp\left(\frac{V + 33}{-8.1}\right)}$	$\frac{1}{1 + \exp\left(\frac{V + 60}{6.2}\right)}$	$2.8 + \frac{14}{\exp\left(\frac{V + 27}{10}\right) + \exp\left(\frac{V + 70}{-13}\right)}$	$120 + \frac{300}{\exp\left(\frac{V + 55}{9}\right) + \exp\left(\frac{V + 65}{-16}\right)}$
I_A	3	$\frac{1}{1 + \exp\left(\frac{V + 27.2}{-8.7}\right)}$	$\frac{1}{1 + \exp\left(\frac{V + 56.9}{4.9}\right)}$	$23.2 - \frac{20.8}{1 + \exp\left(\frac{V + 32.9}{-15.2}\right)}$	$77.2 - \frac{58.4}{1 + \exp\left(\frac{V + 38.9}{-26.5}\right)}$
I_{KCa}	4	$\frac{[Ca]}{[Ca] + 3} * \frac{1}{1 + \exp\left(\frac{V + 28.3}{-12.6}\right)}$		$180.6 - \frac{150.2}{1 + \exp\left(\frac{V + 46}{-22.7}\right)}$	
I_{Kd}	4	$\frac{1}{1 + \exp\left(\frac{V + 12.3}{-11.8}\right)}$		$14.4 - \frac{12.8}{1 + \exp\left(\frac{V + 28.3}{-19.2}\right)}$	
I_H	1	$\frac{1}{1 + \exp\left(\frac{V + 75}{5.5}\right)}$		$2 / \exp\left(\frac{V + 169.7}{-11.6}\right) + \exp\left(\frac{V - 26.7}{14.3}\right)$	

Figure 2.1: Voltage dependence of model currents. V is the membrane potential in mV; $[Ca]$, the intracellular calcium concentration in mM. Absences in the table indicate non-inactivating currents (e.g. $h = 1 \forall V$).

The reversal potentials determines the membrane potential at which a current begins fluxing ions in the opposite direction.

CURRENT	I_{Na}	I_{CaT}	I_{CaS}	I_A	I_{KCa}	I_{Kd}	I_H	I_{leak}
E (mV)	50	*	*	-80	-80	-80	-20	-50

Table 2.1: Reversal potentials for model currents in mV. Calcium reversal potentials vary as a function of voltage and calcium.

The calcium reversal potential is computed from the Nernst potential^{22,56}.

$$E_{Ca} = \frac{RT}{zF} \ln \left(\frac{[Ca^{2+}]_{ex}}{[Ca^{2+}]_{in}} \right) \quad (2.1)$$

where $[Ca^{2+}]_{in}$ is the intracellular calcium concentration in μM and

$[Ca^{2+}]_{ex} = 3 \mu\text{M}$, extracellular calcium concentration

$R = 8.314 \text{ J} \cdot \text{mol/K}$, gas constant

$T = 284.15 \text{ K}$, temperature

$z = 2$, valence of calcium cation

$F = 96485 \text{ C/mol}$, Faraday constant

The calcium concentration evolves with time (Equation 1.5), where

$\tau_{Ca} = 200 \text{ ms}$, calcium buffering time constant

$f = 14.96 \mu\text{M/nA}$, conversion factor

The conversion factor translates calcium currents into a rate of intracellular calcium flux^{42,46}. The factor depends on the ratio of the surface area of the cell to the volume in which the calcium concentration is measured. The buffering zone is taken to be a narrow cylindrical shell just inside the membrane with a diameter of 50 microns and length 400 microns. Finally, the voltage evolves (Equation 1.1) with membrane capacitance $C_m = 10 \text{ nF/mm}^2$ where the surface area of the cell is 0.0628 mm^2 ^{42,54}.

Synapses were modeled as non-inactivating currents according to a standard model⁵⁷. The synaptic current is

$$I_{syn} = g_{syn}s(V_{post} - E_{syn}) \quad (2.2)$$

where V_{post} is the membrane potential of the postsynaptic neuron and E_{syn} is the reversal potential of the synapse. The synaptic gating variable s evolves with time.

$$\frac{ds}{dt} = \frac{s_\infty(V_{pre}) - s}{\tau_{syn}} \quad (2.3)$$

$$s_\infty(V_{pre}) = \frac{1}{1 + \exp \left(\frac{V + V_{th}}{-V_\sigma} \right)} \quad (2.4)$$

$$\tau_{syn} = \tau_d (1 - s_\infty(V_{pre})) \quad (2.5)$$

where

- V_{pre} membrane potential of the presynaptic neuron
- V_{th} half-potential of the synapse
- V_σ describes the slope of the activation curve
- τ_d time constant for transmitter-receptor dissociation
- AB, LP, and PY are glutamatergic neurons whereas PD is cholinergic.

CONSTANT	GLUTAMATERGIC	CHOLINERGIC
E (mV)	-70	-80
V_{th} (mV)	-35	-35
V_σ (mV)	5	5
τ_d (ms)	40	100

Table 2.2: Constants for synaptic currents.

2.2 SIMULATING MODEL NEURONS

Model neurons were simulated with a time step $dt = 0.1$ ms using the exponential Euler method⁴⁵.

$$V_m(t + dt) = V_\infty + (V_m(t) - V_\infty) \exp\left(-\frac{dt}{\tau_V}\right) \quad (2.6)$$

$$V_\infty = \frac{\sum_i g_i(V_m) E_i}{\sum_i g_i(V_m)} \quad (2.7)$$

$$\tau_V = \frac{C_m}{\sum_i g_i(V_m)} \quad (2.8)$$

This method is asymptotically stable, unlike linear Euler and much faster than higher order Runge-Kutta methods. Initial conditions were standardized as follows.

V_m	$[Ca^{2+}]_{in}$	m	h
-65	0.02	0	1

Table 2.3: Initial conditions for typical simulations. Voltage is in mV, calcium concentration is in μ M.

Unless otherwise specified, the first 25% of a simulation was discarded as transient.

2.3 THE PRINZ DATABASE

In order to characterize the solution space for single-compartment AB-PD-like models, all bursting neurons in the database described in

Prinz *et al.* were simulated. Since **AB** neurons continue to oscillate in the presence of sodium channel blockers, **AB**-like models were implemented without spike-producing I_{Na} or I_{CaT} currents. A subset of Prinz models and optimized derivatives produce slow-wave voltage oscillations qualitatively similar to rectified sinusoids in the absence of these inward currents. The database expedited the search for candidate solutions to optimize.

The pyloric network models consist of three cellular compartments, **AB-PD**, **LP**, and **PY**. The intrinsic pacemaker **AB** is strongly electrically coupled to the pyloric dilator cells (**PDs**) and has been reduced to a single-compartment computational composite. All pyloric cells (**PYs**), which are electrically coupled, have been reduced to a single **PY** compartment.

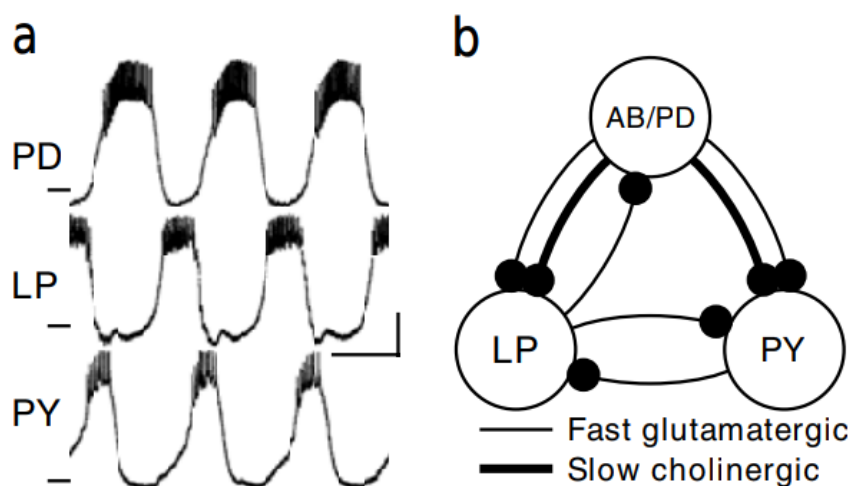


Figure 2.2: Biological pyloric rhythm and pyloric circuit model network. (A) Pyloric rhythm recorded from *H. americanus* with intracellular electrodes. Scale bars, 1 s, and 10 mV; horizontal lines, -60 mV. (B) Schematic of a simplified version of the underlying circuit (Figure 1.2). All synapses are inhibitory⁴⁷.

2.4 MODULATORY INPUT

Sharpe *et al.* and Swensen & Marder fit models of modulatory input current to experimental data. The Swensen model possesses a wider basin of activation without a sharp peak, and is based recordings from the **PD** neuron. While both models fit proctolin data, **RPCH** response more closely resembles the graded activation of Swensen & Marder modulatory input.

Sharp <i>et al.</i> Swensen & Marder		
V_{th} (mV)	-55	-21
V_σ (mV)	5	8
τ_m (ms)	6	6
E (mV)	-10	-22

Table 2.4: Comparison of Sharp and Swensen modulatory input currents.

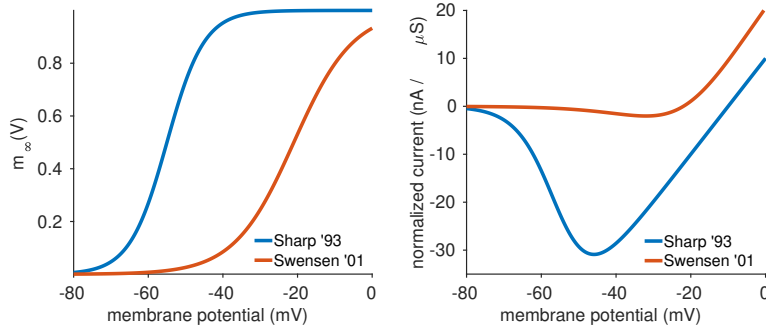


Figure 2.3: Models of modulatory input current. Sharp and Swensen modulatory input current are compared. The left-hand trace shows the activation gating variable steady-state as a function of membrane potential. The right-hand trace shows the IV curves for these model currents.

2.5 MODEL IMPLEMENTATION

In order to quickly simulate many models with varied parameters, we developed simulation software called `xolotl`. This fast single-compartment and multi-compartment simulator is written in C++ with MATLAB wrappers. Designed with a focus on flexibility and speed, it can simulate single-compartment models, networks of these, and detailed multi-compartment models. This novel software has been developed by Srinivas Gorur-Shandilya and the author.

`xolotl` separates neurons into compartments, where each compartment and contained current is fully modular. Synapses link two compartments together. Compartments can contain any number of parameters and variables so that `xolotl` is readily adaptable to any number of simulation regimes. Since a main benefit of modeling is generating a large number of *in-silico* experiments to support or generate hypotheses, `xolotl` objects can be passed through optimization protocols to develop sets of parameter values which satisfy arbitrary biological constraints. Many models can be generated which replicate biological behavior; since STG neurons are degenerate with respect to maximal conductance density and conductance density can be assumed constant on non-homeostatic timescales, maximal conduc-

xolotl is the Aztec god of lightning and death

tances of intrinsic and synaptic currents serve as readily optimized parameters for single cell and network models.

Maximal conductances for intrinsic currents were bound by the interval $[0.1, 2000] \mu\text{S}/\text{mm}^2$ and synaptic conductances were bound by $[0.1, 100] \mu\text{S}/\text{mm}^2$, keeping with Prinz *et al.* Injected modulatory input current in dynamic clamp experiments typically lies in the range $[0, 100] \text{nS}$. For this reason, maximal conductance density for I_{MI} was bounded by the interval $[0, 1] \mu\text{S}/\text{mm}^2$ since

$$1 \mu\text{S}/\text{mm}^2 \times 0.0628 \text{ mm}^2 \times \frac{1000 \text{ nS}}{1 \mu\text{S}} = 62.8 \text{ nS}$$

Similarly, Swensen & Marder report the maximal steady-state current in **PD** cells to be -1.8nA . A modeled maximal conductance of $1.0 \mu\text{S}/\text{mm}^2$ would produce a current of -2.0nA .

2.5.1 Parameter Optimization

The first step in any parameter optimization algorithm begins with the cost function $f : \mathbb{R}^n \rightarrow \mathbb{R}$. The function accepts a candidate solution in the form of a vector of real numbers and produces a real output, which represents the objective function value of the candidate solution. This process is necessary to objectively and unambiguously evaluate the fitness of a model by reducing the high-dimensional parameter set and the complicated non-analytical function which produces the resultant waveforms into a single real number. Optimization algorithms aim to discover candidate solutions which produce low costs, where a cost of zero signifies a model which fits the cost function perfectly. Since the **STG** is highly degenerate in ion channel expression, maximal conductances are the targeted parameters. The solution space has been loosely characterized, producing a large number of parameter seeds to optimize.

We built an optimization toolbox, **procrustes**, which optimizes any parameters passed to it based on an arbitrary cost function. The interface serves as front-end for several parameter optimization algorithms used to develop models with desired metrics. Since application of **RPCH** increases the burst frequency and maximum of the slow-wave oscillations in **PD** and **LP** cells, increases in these metrics over increasing modulatory input is strongly targeted. We tested **procrustes** with three parameter optimization algorithms: gradient descent, a genetic algorithm, and particle swarm optimization.

The simplest, gradient descent, is a first-order iterative algorithm in which candidate solutions take steps proportional to the gradient of the cost function at the current point. This method can readily be applied to high-dimensional spaces, though can be inefficient. Close to the minimum, gradient descent tends to “zig-zag” in parameter space. For a cost landscape with many local minima, many seeds

procrustes is a bandit of Greek mythology who forced his victims to fit into a bed, by stretching and amputating

with diverse parameter values must be used in order to effectively characterize possible solutions.

A genetic algorithm combines a gradient descent methods with stochastic “mutation,” in which solutions are combined or transformed to produce better ones. This has the advantage of more readily finding substantial local minima, but escaping from superficially fit solutions. Unfortunately, genetic algorithms are computationally expensive and suffer in problem domains with a complex cost landscape.

Particle swarm optimization relies on the generation of many candidate solutions (“particles”) which move in parameter space towards the best position of a particle in the swarm. Since the parameter space is widely sampled by the stochastically-generated particles, particle swarm optimization can efficiently handle complex cost landscapes and high-dimensional parameter spaces. Particle swarm optimization is especially effective in this case since solutions can be readily screened for non-bursting, non-triphasic activity and rejected by the swarm.

Regardless of algorithm, the greatest difficulty is almost always writing a sufficient cost function, which arrives at suitable solutions within appreciable time. Since no general technique exists for producing Lyapunov functions for ordinary differential equations; the cost function must be designed manually. A good cost function consistently produces models which satisfy the researcher’s needs in efficient time. While the cost function must be ambiguous with respect to the constraints of optimization, the construction of the function and evaluation of resultant models is entirely arbitrary. [Figure 2.4](#) shows that optimization can arrive at suitable solutions in a short period of time, provided that an efficient and unambiguous cost function is implemented.

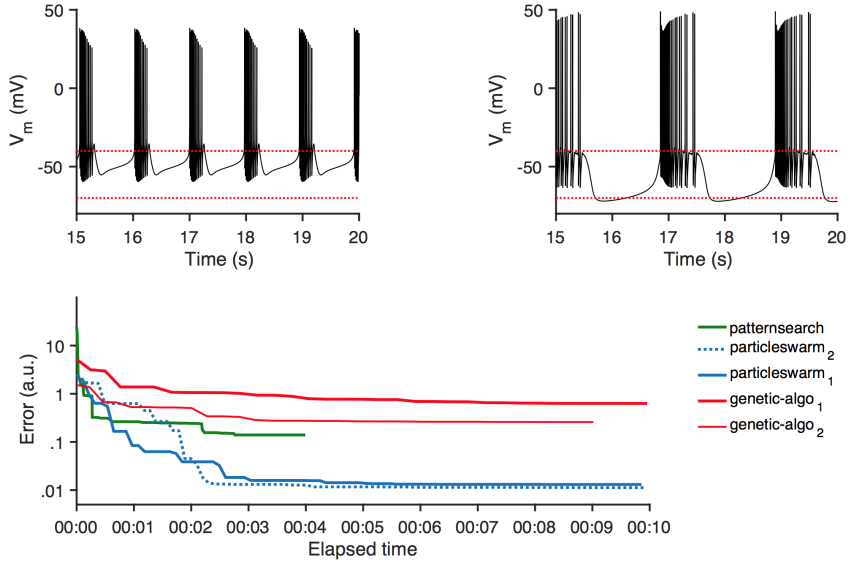


Figure 2.4: Particle swarm optimization finds high-dimensional neuronal models with arbitrary constraints faster than other common algorithms. The top left trace displays a single-compartment seed. The top right trace displays the solution after optimization. Metrics for optimization were burst-frequency of 0.5 Hz, duty cycle of 0.3, and a slow wave bounded by $[-70, -40]$ mV where the spike troughs are above the slow wave. The bottom trace shows three optimization algorithms beginning with the same seed. Optimization terminates after 10 min or at a local minimum, as set by optimizer options. Figure by S. Gorur-Shandilya.

2.5.2 Computing Metrics

Simulation of a conductance-based model elicits voltage and calcium traces. The peaks of the calcium trace indicate the points of greatest spike density in the voltage traces. For a stationary signal, the burst period is the mean time between calcium peaks. The duty cycle is the ratio between burst duration and burst period. The time between the end of a burst of one cell and the beginning of a burst in another cell is the gap. Similarly, the delay is the time from a start of one burst in one cell to the beginning of a burst in another.

$$\text{burst period} = \text{mean}(\text{calcium peaks}) = \frac{1}{\text{burst frequency}} \quad (2.9)$$

$$\text{duty cycle} = \frac{\text{burst duration}}{\text{burst period}} \quad (2.10)$$

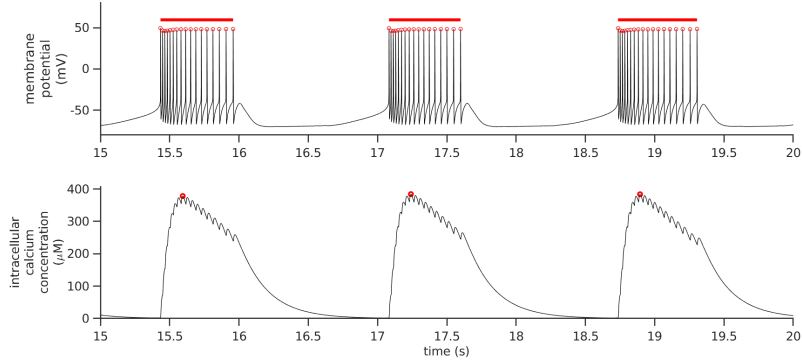


Figure 2.5: Estimating burst metrics. On the top trace, red dots show spike peak locations. The red bar indicates the burst duration. The bottom trace displays red dots at the calcium peaks.

2.5.3 Designing the Cost Function

For evaluations of three-compartment network models, the cost function computes the cost, burst frequency, duty cycle, mean spikes per burst, and the global minimum and maximum of the slow wave at several values of modulatory input into one or more cells.

First the function evaluates whether the model elicits network activity within normal limits for real pyloric circuits. Once this has been confirmed at all steps of modulatory input current, the model targets ratios in various metrics to fine-tune solutions towards target activity.

2.5.3.1 Evaluate Models for Pyloric Activity

The first step confirms that the model is triphasic and pyloric. Burst periods, mean spikes per burst, burst durations, duty cycles, inter-burst periods, and delay between the starts of each burst were computed. If within an acceptable range, the cost was set to zero and penalized by a normalized cost if outside the range. This range is set by experimental results. Normal pyloric networks fall within the following bounds.

For a value v and target bounds b_{low} , b_{high} , the computed cost is

$$\text{cost} \propto 1 - \left| \frac{b_{high} - b_{low}}{b_{high} + b_{low} + 2v} \right| \quad (2.11)$$

outside the bounds and zero within bounds. The first 50% (10 s) of simulation were discarded as transient and spike times were computed by positive crossings of the zero line. If the network is bursting with an appropriate number of spikes, the model is checked for depolarization block, in which the membrane is depolarized but cannot spike. The voltage between each spike is recorded and each inter-spike interval within the burst is checked against the mean inter-spike

METRIC	LOWER	UPPER
calcium peak coefficient of variation	0	0.1
burst period (s)	0.3	2
spikes per burst	4	30
burst duration (s)	0.2860	1.4
duty cycle	0.2050	0.4250
inter-burst period from AB-PD to LP (s)	0.112	0.33
inter-burst period from LP to PY (s)	-0.121	-0.001
delay from AB-PD to LP (s)	0.6340	0.9720
delay from AB-PD to PY (s)	0.9250	1.3570

Table 2.5: Pyloric network metric bounds.

interval for the burst to confirm that the compartment is regularly spiking during the burst. If any of these tests fail, the cost function returns a high cost and the exits the simulation.

There are several advantages to this preliminary step. First, the high cost guarantees that the failing candidate solution will not be the lowest-cost solution in the swarm, meaning that other models will not repeat the same optimization steps. Second, exiting the simulation saves time, since this solution will be discarded in any case.

As initial parameters for parameter optimization over response to modulatory input, 1,148 network models with a cost of zero in the decentralized condition were used. This dataset is available upon request.

2.5.3.2 Response to Modulatory Input

If candidate solutions pass pyloricity tests in the modulated and decentralized cases, the solution is further refined. The burst frequency, duty cycle, mean number of spikes per burst, and minimum and maximum of the slow wave are computed. A Savitzky-Golay filter with a window size of 300 ms is used to determine the maximum of the slow wave. In all other cases, the raw trace is used.

The ratio between metrics in the modulated and decentralized case are computed. Targeting a ratio has several benefits. First, it is agnostic to initial neuron parameters. For instance, burst frequencies in healthy pyloric circuits commonly vary on the interval [0.5, 1.5] Hz between preparations²⁶. By computing a ratio, the response is normalize to the basal activity of the model, preventing over-fitting. In addition, examining two values of maximal conductance, rather than a series of linearly-spaced values significantly cuts down on computational complexity. While only two points were specified in the ratio, the constraint of pyloricity means the cost function strongly favors

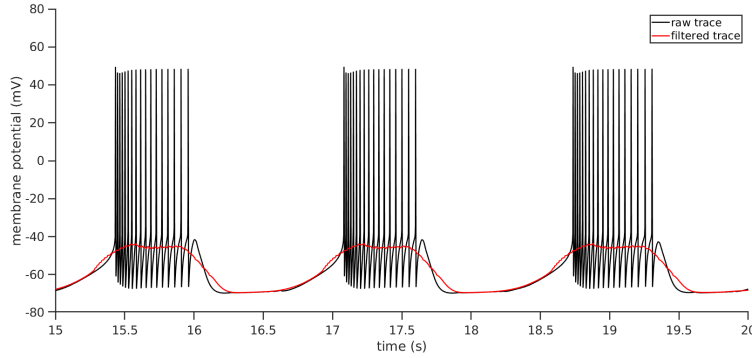


Figure 2.6: Estimating slow wave maxima using a first-order Savitzky-Golay filter with a window of 300 ms applied to the voltage trace of a bursting neuron. A Savitzky-Golay filter is a convolutional digital filter which fits sub-sets of adjacent data to a low-degree polynomial by the least squares method. This has the effect of smoothing high-amplitude, high-frequency oscillations, without strongly distorting low-frequency signal components⁵⁸.

METRIC	RATIO	CHANGE
burst frequency	1.5	
duty cycle	1.0	
slow wave maximum		+5 mV
slow wave minimum		-5 mV

Table 2.6: Pyloric network metric target ratios and changes between the modulated and decentralized cases.

models with graded increase with respect to increasing modulatory input. For single-neuron simulations, this constraint does not exist.

Because the change in slow wave amplitude is a signed quantity, the slow wave maximum towards a +5 mV increase instead of a rational change.

Graded increases, where the cost is summed for each point along the I_{MI} maximal conductance range, was only used for single-neuron fitting of models to dose-response data. In this regime, metric values are specified for each value of modulatory input maximal conductance. This method has the advantage of increasing the cost on models which do not exhibit graded responses to modulatory input, but is computationally expensive and may result in over-fitting.

3

RESULTS

Decentralized **STG** preparations have descending modulatory inputs from the **CoGs** and **OG** removed. **STG** neurons in a decentralized state exhibit a slower burst frequency and variable network activity^{20,52}. This effect can be restored to normal function by exogenous application of modulatory substances into the saline bath^{37,39}. Proctolin and **RPCH** are neuromodulators which open a mixed cation inward modulatory input current modulatory input current (I_{MI})³⁹.

To model decentralization and modulation, single-neuron anterior burster cell (**AB**) models and network (**AB-PD**, **LP**, **PY**) models were constructed according to the Hodgkin-Huxley formalism^{43,46,47,53,54}. Maximal conductances were determined by particle swarm optimization ([Section 2.5.1](#)) to respond to modulatory input in the form of I_{MI} ³⁹. **AB** and the two **PD** cells were combined into a computational composite **AB-PD** since the cells are strongly electrically coupled ([Figure 2.2](#)). Similarly, electrically-coupled **PY** cells were combined into a single computational composite, following Prinz *et al.*⁴⁷. The **AB-PD** pacemaker kernel synapses onto **LP** and **PY** with inhibitory glutamatergic and cholinergic synapses. **LP** and **PY** reciprocally inhibit each other and **LP** feeds back onto the pacemaker kernel ([Figure 1.1](#)).

AB increases in frequency and amplitude from baseline in bath-applied proctolin^{33,37–39}. Modulatory input conductance ([Section 2.4](#)) was added to single-compartment models from the Prinz database⁴⁶ to characterize the effect of I_{MI} on a population of previously studied models. Most models did not respond to I_{MI} , so maximal conductances were manipulated in a particle swarm optimization protocol to produce models which increase in frequency and amplitude to increasing I_{MI} maximal conductance^{36,37}.

RPCH activates a modulatory input conductance in **AB** and **LP** cells. Network models were simulated under I_{MI} conductance in **AB-PD**, **LP** and both model neurons to simulate neuromodulation by **RPCH**. Maximal conductances of the three model neurons and synapses were manipulated by particle swarm optimization to produce models with slow, unstable rhythms in the decentralized condition and increased burst frequency and amplitude under neuromodulation. While modulation onto the pacemaker and **LP** recapitulated experimental findings ([Figure 1.4](#)), modulation into **AB-PD** and **LP** produced the most stable rhythms.

3.1 MODULATION IN AB MODELS SWITCHES BETWEEN AMPLITUDE STATES

To develop an initial set of solutions to optimize (the “seed”), neurons from the **STG** neuron database were simulated⁴⁶. This database contains 2.2 million model neurons with linearly spaced parameters. Neurons flagged as “bursting neurons” were simulated with increasing levels of modulatory input. Since **AB** does not fire strong action potentials (Figure 1.5) and responds to **RPCH** under the potent sodium channel blocker **TTX**, I_{Na} and I_{CaT} maximal conductances set to zero to eliminate sodium and calcium spikes respectively³⁶. These models would serve as a testbed for exploring neuromodulation in isolated cells.

Quiescent models were defined as having amplitude < 20 mV to isolate models that appear similar to decentralized preparations in tetrodotoxin (**TTX**)³⁶. Slow wave amplitude was defined as the maximal peak voltage minus the minimal trough voltage at steady-state ($10 \text{ s} < t < 20 \text{ s}$).

Modulatory input was applied to these low-amplitude oscillators ($n = 14,700$), which were simulated for 20 s (Figure A.1). The first 10 s were discarded as transient and burst frequency and amplitude were computed. To test sensitivity to initial conditions, the simulations were repeated with $V_m = 60 \text{ mV}$ and $m_{MI} = 1$ instead of standard initial conditions (Table 2.3). No significant differences were observed.

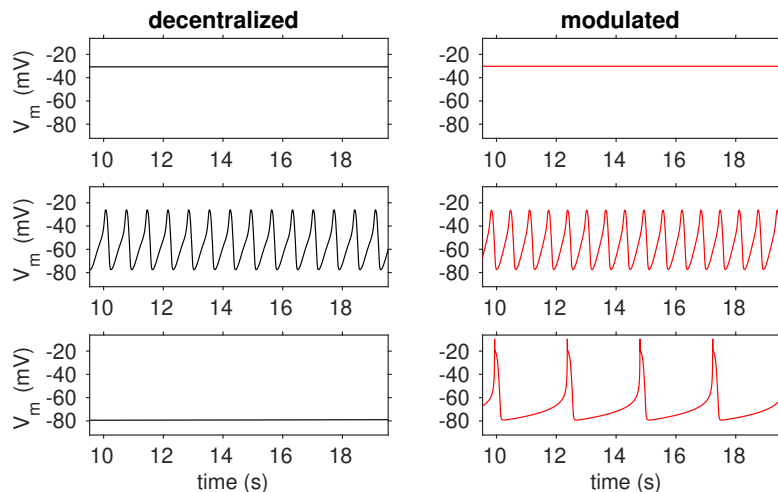


Figure 3.1: Three motifs of modulation in model **AB** neurons from the **STG** database. Most model neurons from the Prinz **STG** database without I_{Na} or I_{CaT} conductance remained quiescent. A subset of models oscillated in both conditions and < 100 switched from quiescence to oscillation. Black traces demonstrate the non-modulated case and red traces indicate $\bar{g}_M I = 1 \mu\text{S}/\text{mm}^2$.

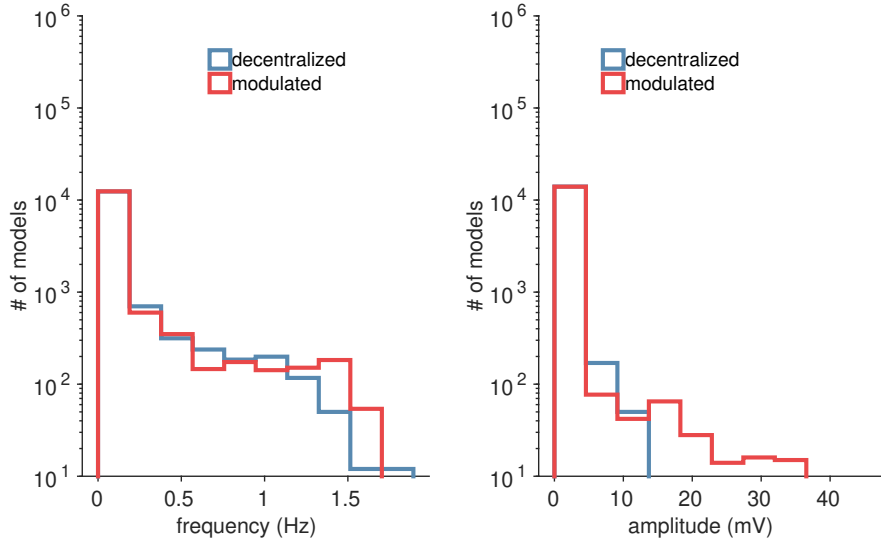


Figure 3.2: Most database models without I_{Na} or I_{CaT} do not respond to modulatory input.

Only a small subset of the models exhibited changes burst frequency and amplitude (Figure 3.2). Figure 3.1 illustrates three motifs in order of rarity. Most commonly, models with and without modulatory input were quiescent. A subset of models exhibited subthreshold voltage oscillations in both decentralized and modulated cases. The 1000 models with the greatest change in frequency and amplitude were replotted (Figure A.2). Models exhibit a sharp increase in peak voltage over a small range of modulatory input. Frequency increases monotonically sudden jumps in magnitude.

The 100 models which responded to modulatory input in a graded manner with increasing frequency and amplitude were optimized using a gradient descent algorithm (Figure A.3). Since the modulatory input IV curve achieves maximal inward current at $V_m \approx -32$ mV, peak voltage at high values of I_{MI} maximal conductance tended to be at least this membrane potential. A subset of models achieved graded frequency increase, though amplitude showed a sharply peaked jump from small oscillations (< 10 mV) to amplitude indicative of biological AB neurons (Figure A.3). These data suggest that a subset of models experience modulatory input current as a bistable switch between non-oscillatory and oscillatory states.

When models were optimized over a smaller range of I_{MI} maximal conductance ($\bar{g}_{MI} = [0, 0.2] \mu S/mm^2$), resultant solutions responded to modulatory input in a graded manner. The burst frequency and amplitude increase smoothly as functions of modulatory input, responding most strongly at low maximal conductance. We hypothesize several reasons for this effect. First, the total capacitance of a physiologically-realistic AB neuron is much higher than in the model neurons used here^{40,44}. Second, the elimination of several currents sig-

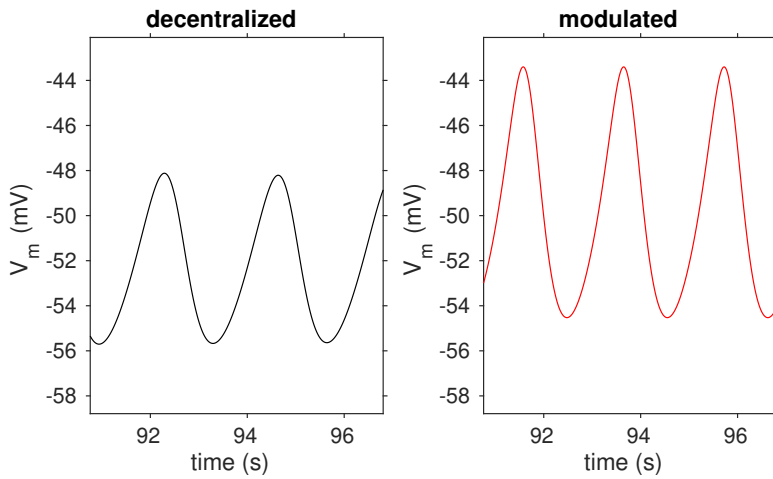


Figure 3.3: AB model increases in amplitude and frequency with modulatory input. The model recapitulates electrophysiological recordings (Figure 1.5). Modulatory input current cannot replace slow calcium in its excitatory role, but a balance between I_H , I_{CaS} , and outward currents produce the conditions for I_{MI} to depolarize the membrane potential during voltage peaks.

nificantly reduced the input resistance so that I_{MI} contributes a greater proportion to the net instantaneous current. Thirdly, most solutions converged to small values of conductances. Since the membrane potential evolves proportionally to the instantaneous sum of the currents, relative proportions of conductance with respect to each other and the membrane capacitance determine the dynamics. A model neuron with small membrane capacitance and intrinsic conductances produces qualitatively different activity with smaller perturbations.

3.2 VARIABILITY IN NETWORK RESPONSE TO MODULATION

RPCH activates I_{MI} in the anterior burster (AB) and lateral pyloric (LP) cells of the STG³⁶. To model the effects of RPCH modulation in the pyloric circuit, I_{MI} was added to each cell and together in the network model (Figure 1.3) with AB and PDs reduced to a single composite pacemaker neuron (AB-PD). Particle swarm optimization (Section 2.5.1) selected for models which increased in burst frequency and slow wave amplitude over increasing modulatory input into AB-PD, LP, and both model neurons. Maximal conductances for all ionic and synaptic currents were varied as parameters (28 parameters plus one for each cell with I_{MI}).

3.2.1 Neuromodulation Increases Frequency and Amplitude

Optimization produced models of the network with increased burst frequency and slow wave amplitude under modulation in the three

conditions. Three motifs of network activity appeared several times in optimized solutions. Some model networks produced triphasic activity without modulation, and increased burst frequency and slow wave amplitude under neuromodulation. Others produced periodic, but not pyloric activity (e.g. skipped bursts) and rectified these errors under modulation. The third category contained quiescent and tonically-firing networks which become pyloric under modulation.

[Figure 3.4](#) displays an optimized network model with modulatory input into [AB-PD](#). Without modulation, the network is stable, with a triphasic rhythm. Addition of modulatory input monotonically increases the burst frequency. The duty cycle for [PY](#) decreases from 0.5 to 0.3. Similarly, the mean number of spikes per burst in [PY](#) decreases. This indicates that the burst duration is decreasing and the mean inter-spike interval remains relatively constant. [PY](#) is not able to increase in slow-wave amplitude until the duration and intensity of the bursts can be maintained at the higher frequency.

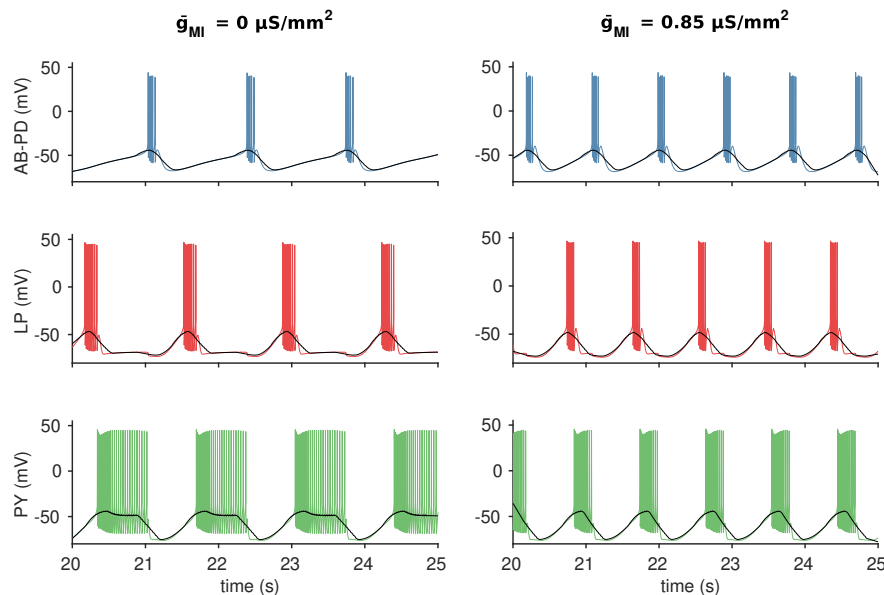


[Figure 3.4](#): Modulation into [AB-PD](#) increases burst frequency and [AB-PD](#) slow wave amplitude. Left-hand traces are without neuromodulation.. Right-hand traces have I_{MI} in [AB-PD](#) at $\bar{g}_{MI} = 0.85 \mu\text{S}/\text{mm}^2$. Colors indicate cells (blue is [AB-PD](#), red is [LP](#), green is [PY](#) and overlaid black indicates the slow wave).

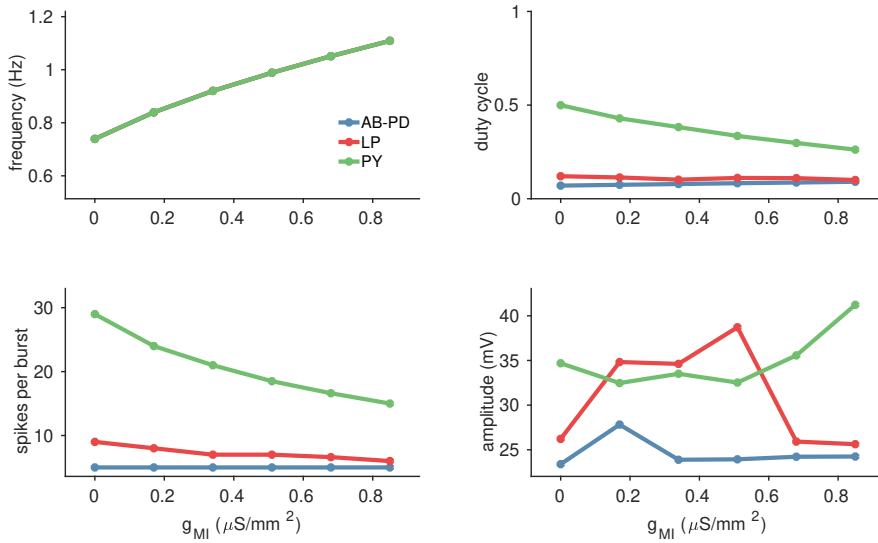


Figure 3.5: Modulation into AB-PD increases burst frequency and AB-PD slow wave amplitude. Metrics at steady-state as a function of increasing modulatory input. Colors indicate cells (blue is AB-PD, red is LP, green is PY).

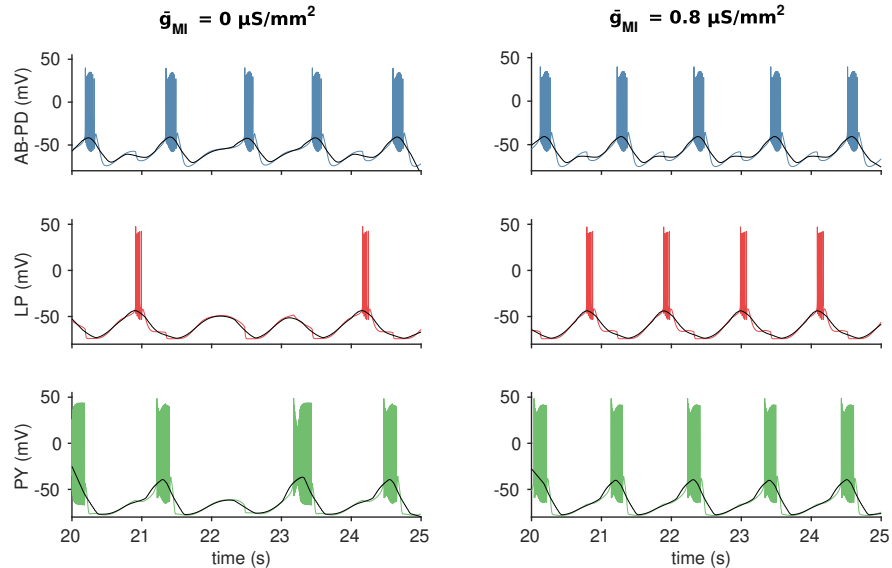


Figure 3.6: Modulation into LP rescues abnormal activity. Modulation into LP increases burst frequency and AB-PD slow wave amplitude. Left-hand traces are without neuromodulation. Right-hand traces have I_{MI} in LP at $\bar{g}_{MI} = 0.8 \mu S/mm^2$. Colors indicate cells (blue is AB-PD, red is LP, green is PY and overlaid black indicates the slow wave).

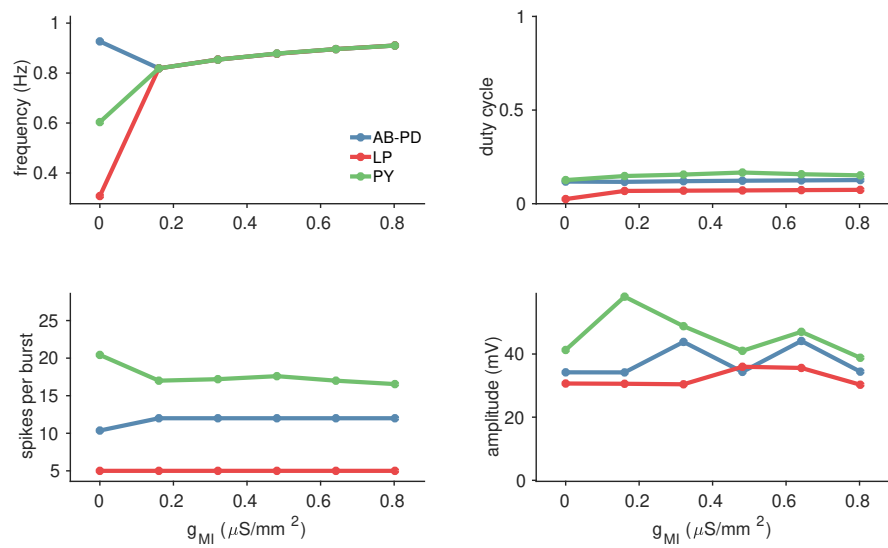


Figure 3.7: Modulation into LP rescues abnormal activity. Modulation into AB-PD increases burst frequency and AB-PD slow wave amplitude. Metrics at steady-state as a function of increasing modulatory input. Colors indicate cells (blue is AB-PD, red is LP, green is PY).

Models can recapitulate loss of triphasic rhythm with decentralization. In Figure 3.6, modulation into **LP** corrects a network with burst asymmetry. After the network is brought back into rhythm, increasing modulation increases the burst frequency. Since all bursts are short in duration, the duty cycle does not change. The slow wave amplitude in **AB-PD** depends on the phase relationship between **AB-PD** and **LP**, which itself depends on the maximal conductance of I_{MI} in **LP**. When the burst in **LP** occurs immediately following the termination of the burst in **AB-PD**, allowing more time between the termination of the burst in **LP** and the next in **AB-PD** the amplitude in the pacemaker is greater.

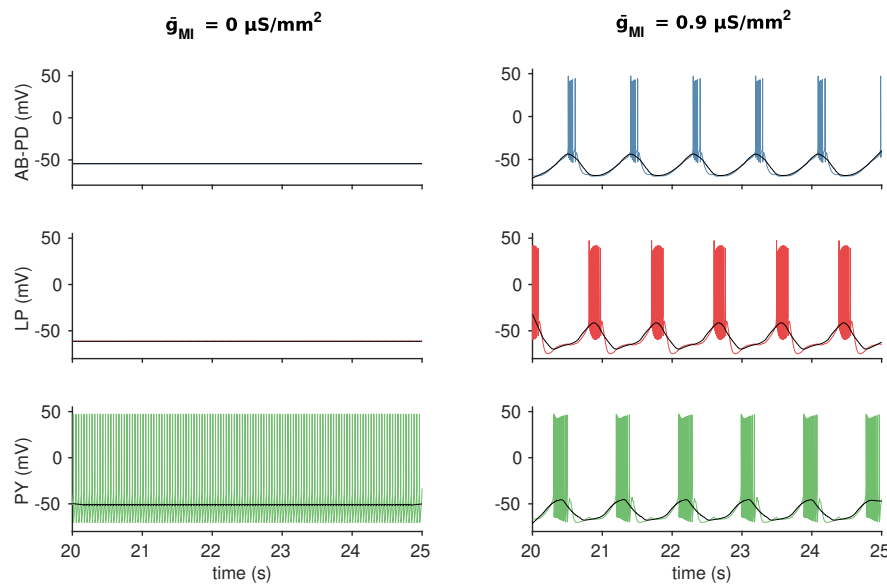


Figure 3.8: Modulation onto **AB-PD** produces triphasic network activity in a quiescent network model. Modulation of the pacemaker increases burst frequency and **AB-PD** slow wave amplitude. Left-hand traces are without neuromodulation.. Right-hand traces have I_{MI} in **AB-PD** at $\bar{g}_{MI} = 0.9 \mu\text{S}/\text{mm}^2$. Colors indicate cells (blue is **AB-PD**, red is **LP**, green is **PY** and overlaid black indicates the slow wave).

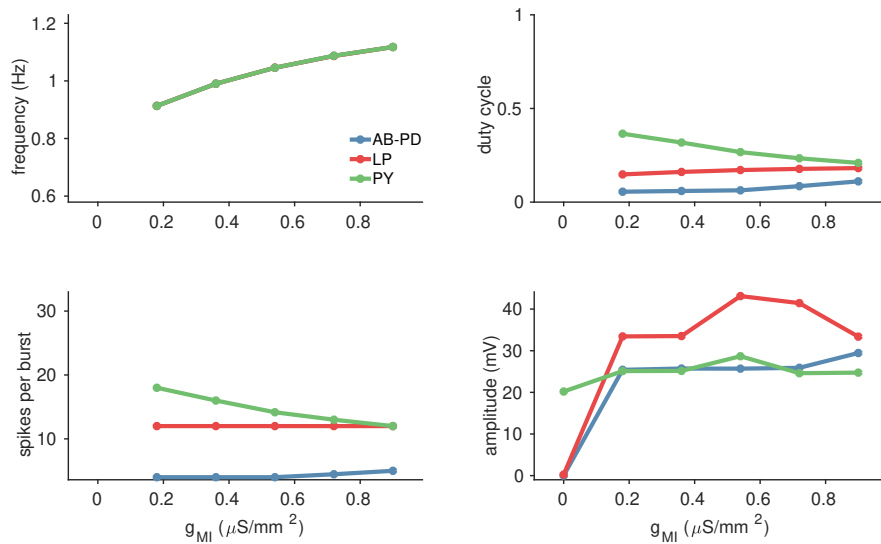


Figure 3.9: Modulation onto AB-PD produces triphasic network activity in a quiescent network model. Modulation of the pacemaker increases burst frequency and AB-PD slow wave amplitude. Metrics at steady-state as a function of increasing modulatory input. Colors indicate cells (blue is AB-PD, red is LP, green is PY).

Figure 3.8 shows quiescence in the decentralized state and normal triphasic activity with modulation in both the pacemaker and LP. Monotonic increase in burst frequency and decrease in duty cycle for models above 0.3 can be seen here as well.

These models qualitatively reproduce slower, variable rhythms in decentralized preparations that recover with activation of I_{MI} in AB, PD, or LP.

3.2.2 Modulation of AB-PD and LP Promotes Robust Pyloric Rhythms

Modulatory input conductance was applied to AB-PD and LP model neurons separately and together at differing strengths. Of the 146 models examined, 87 were optimized for pacemaker modulation, 29 for LP modulation, and 30 for I_{MI} in AB-PD and LP. When models which were triphasic during decentralization were removed, more networks recovered pyloric rhythmicity under modulation of the pacemaker and LP than the pacemaker or LP alone (Figure 3.14).

We hypothesized that this effect is caused by the effectiveness of post-inhibitory rebound as a mechanism for stabilization of central patterns. AB-PD and LP mutually inhibit each other. Phasic excitation applied to each network component during the rising phase of the slow wave would then drive the network through enhanced mutual inhibition.

The role of AB and PDs as the pacemaker kernel is recapitulated in these models. Modulation onto AB-PD more strongly drives network

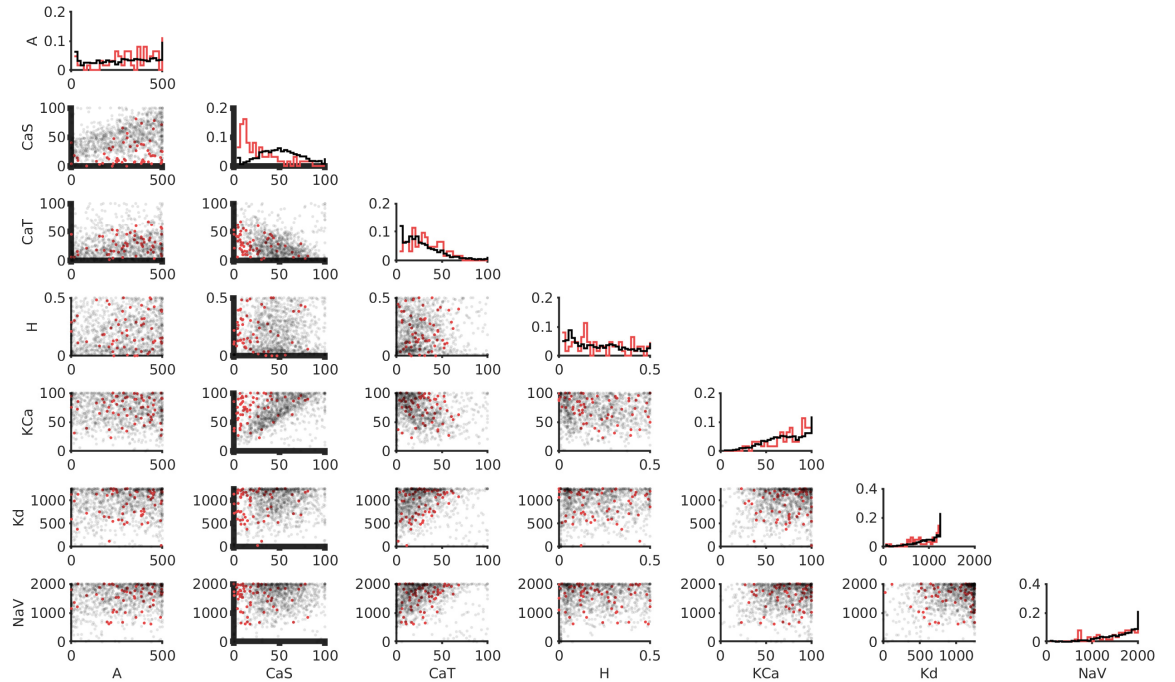


Figure 3.10: Cross-correlation in AB-PD maximal conductances from network models. Maximal conductances from control networks (black, $n = 1,148$), which are pyloric in decentralized conditions, and optimized models (red, $n = 82$), which are non-pyloric in decentralized conditions and pyloric under modulation onto AB-PD and LP, are plotted against each other. Plots on the diagonal are histograms of maximal conductance normalized to population size in each case. **Bold** axes indicate significant correlation (Kolmogorov-Smirnov 2-tailed 2-D test, $p < 0.05$). All conductances are in $\mu\text{S}/\text{mm}^2$.

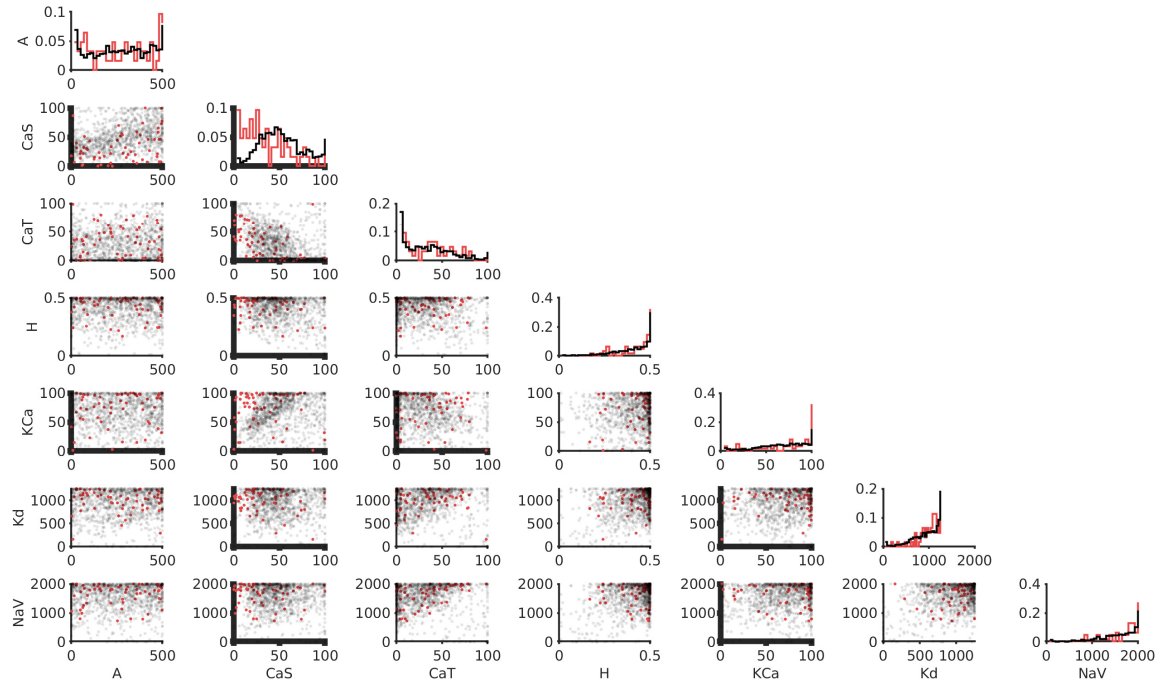


Figure 3.11: Cross-correlation in LP maximal conductances from network models. Maximal conductances from control networks (black, $n = 1,148$), which are pyloric in decentralized conditions, and optimized models (red, $n = 82$), which are non-pyloric in decentralized conditions and pyloric under modulation onto AB-PD and LP, are plotted against each other. Plots on the diagonal are histograms of maximal conductance normalized to population size in each case. **Bold** axes indicate significant correlation (Kolmogorov-Smirnov 2-tailed 2-D test, $p < 0.05$). All conductances are in $\mu\text{S}/\text{mm}^2$.

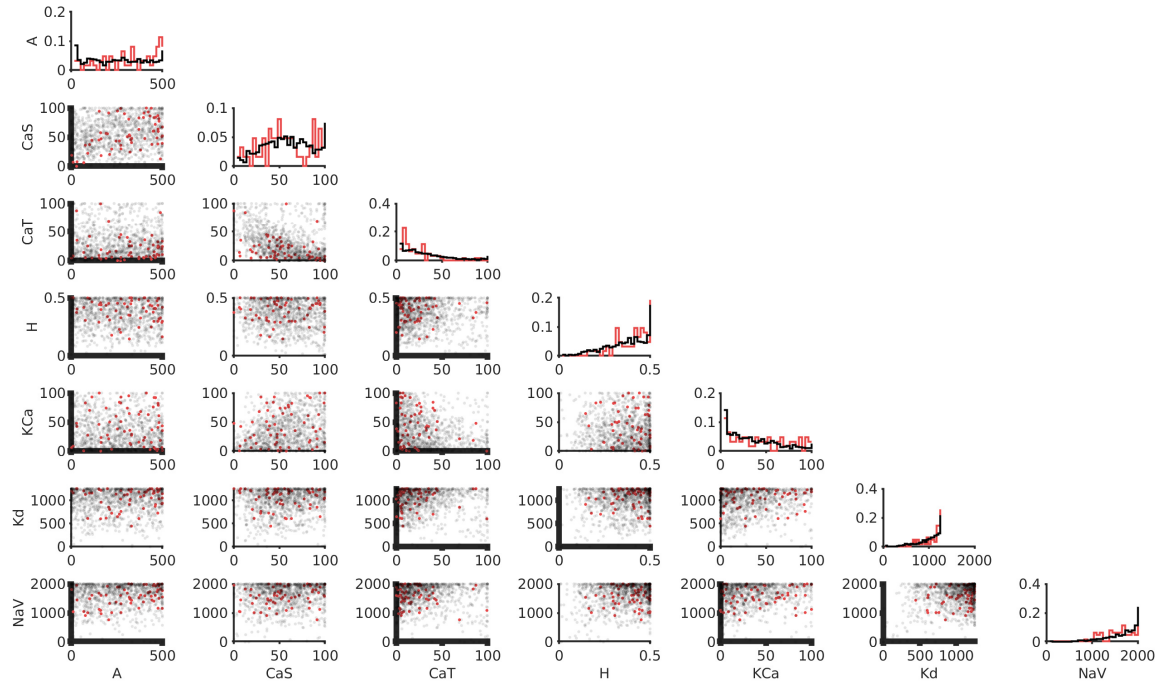


Figure 3.12: Cross-correlation in PY maximal conductances from network models. Maximal conductances from control networks (black, $n = 1,148$), which are pyloric in decentralized conditions, and optimized models (red, $n = 82$), which are non-pyloric in decentralized conditions and pyloric under modulation onto AB-PD and LP, are plotted against each other. Plots on the diagonal are histograms of maximal conductance normalized to population size in each case. **Bold** axes indicate significant correlation (Kolmogorov-Smirnov 2-tailed 2-D test, $p < 0.05$). All conductances are in $\mu\text{S}/\text{mm}^2$.

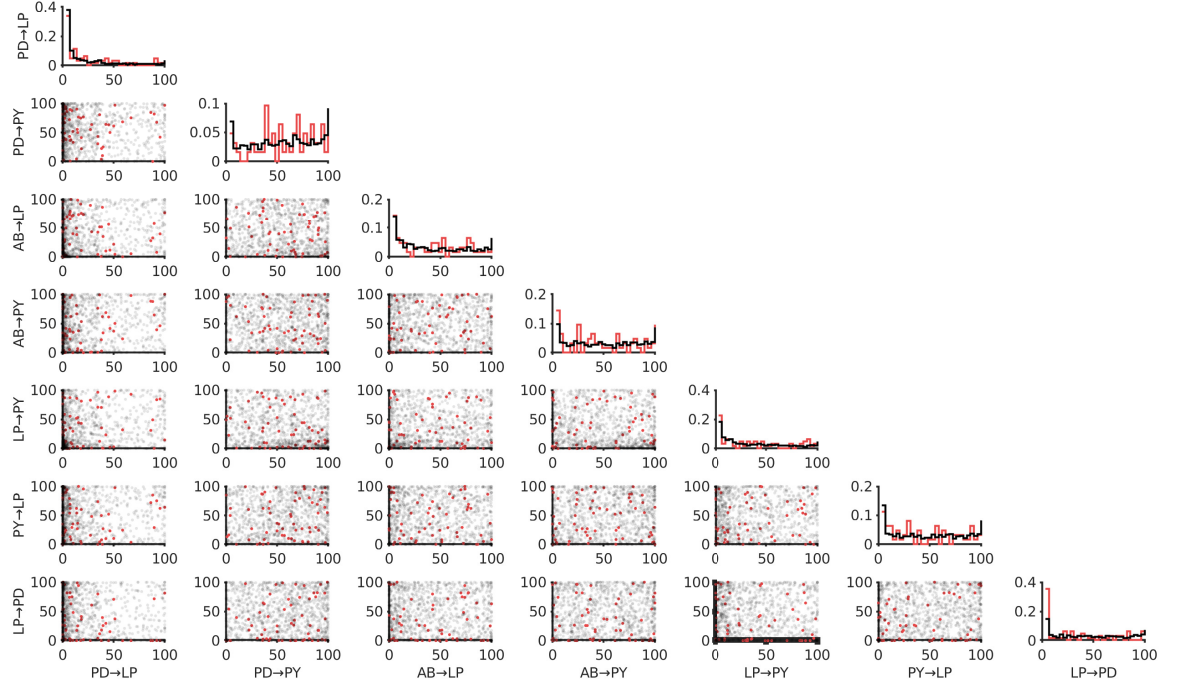


Figure 3.13: Cross-correlation in synaptic maximal conductances from network models. Arrows point from presynaptic to post-synaptic neurons. All synapses are inhibitory and glutamatergic except for synapses from **PD** which are cholinergic. Maximal conductances from control networks (black, $n = 1,148$), which are pyloric in decentralized conditions, and optimized models (red, $n = 82$), which are non-pyloric in decentralized conditions and pyloric under modulation onto **AB-PD** and **LP**, are plotted against each other. Plots on the diagonal are histograms of maximal conductance normalized to population size in each case. **Bold** axes indicate significant correlation (Kolmogorov-Smirnov 2-tailed 2-D test, $p < 0.05$). All conductances are in $\mu\text{S}/\text{mm}^2$.

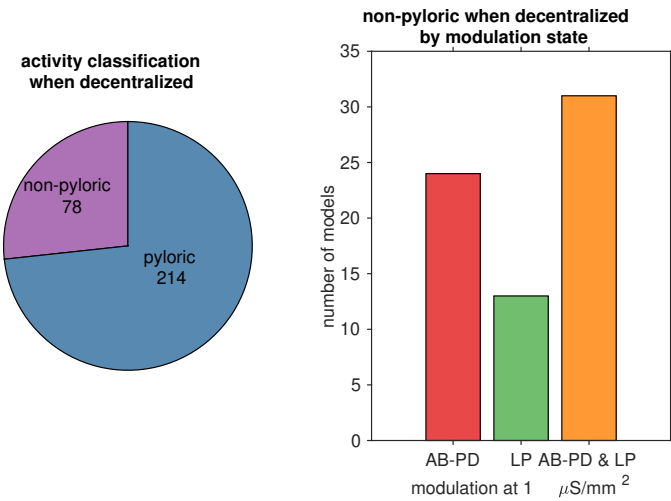


Figure 3.14: Distribution of triphasic network models by modulation state ($n = 146$). Left: Most triphasic models have I_{MI} in the pacemaker kernel and LP, representing intact descending modulation, though many optimized models are triphasic in the decentralized state. This is due to optimization selecting for pyloric-like models *prima facie*. Right: When models which are triphasic in the decentralized state are excluded, most parameter sets result in triphasic networks with modulation and aberrant networks when decentralized.

activity than modulation onto LP. Models were classified as pyloric or non-pyloric in the four cases of modulation (decentralized, AB-PD, LP, both). Correlations between classified network activity in these states reveals strong correlation between AB-PD and AB-PD & LP modulation states (Table 3.1).

To identify specific conductances important in models which respond to I_{MI} , correlations between maximal conductances from model networks which were non-pyloric in decentralized conditions, and pyloric with I_{MI} in AB-PD and LP were computed. The 1,148 pyloric models from which the 146 networks were optimized for response to modulatory input were used as control data (Section 2.5.1). Maximal conductances for the three model neurons and seven synapses were plotted in cross-correlation diagrams (Figure 3.10, Figure 3.11, Figure 3.12, Figure 3.13).

Two-sample, two-tailed two-dimensional Kolmogorov-Smirnov tests were used to determine significance⁵⁹. Significant correlations were found between I_{Cas} and all other conductances ($p < 0.05$) in AB-PD models. We hypothesize that since slow-wave calcium is responsible for burst propagation, models with low slow-calcium conductance are more responsive to neuromodulation in the form of I_{MI} , an inward current which activates near the peak of the slow wave. LP model neurons also show reduced slow-wave calcium maximal conductance in comparison to the control networks. In addition, low I_{Cas} co-occurs

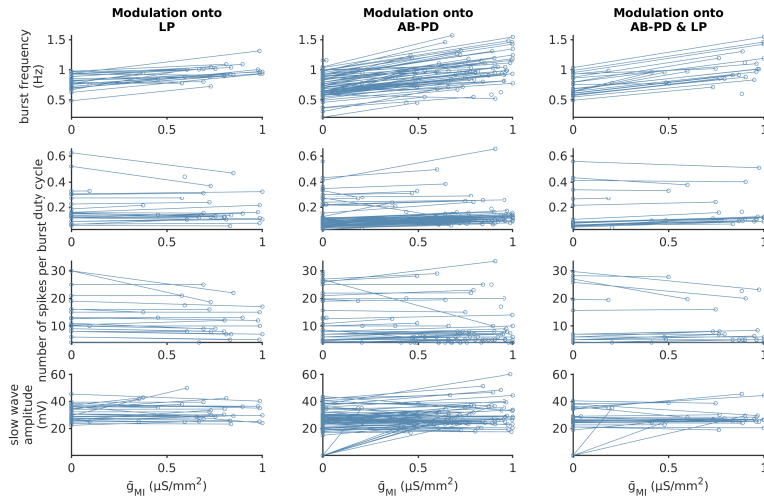


Figure 3.15: 146 network models in decentralized and modulated cases show increased burst frequency and amplitude under modulated conditions with respect to decentralized. Modulation under AB-PD and LP produces the most regular triphasic output. Colors indicate cells (blue is AB-PD).

with high I_{KCa} and I_H . I_{KCa} activates during burst termination and I_H rectifies hyperpolarization. Strong after-burst hyperpolarization, coupled with modulation- and I_H -mediated recovery would explain the increase in burst frequency and amplitude seen with I_{MI} activation. In PY, higher I_{CaS} , I_H , and LP to PY inhibitory synapse maximal conductances indicate strong excitability with post-inhibitory rebound. PY is not modulated by RPCH and must burst in response to inhibitory synaptic feedback.

	DEC.	AB-PD	LP	AB-PD & LP
DEC.	1	0.1986	0.4773	0.1990
AB-PD	0.1986	1	0.0600	0.6751
LP	0.4773	0.0600	1	0.09702
AB-PD & LP	0.1990	0.6751	0.09702	1

Table 3.1: Correlation between models under modulation regimes classified as pyloric or non-pyloric demonstrates the role of the AB-PD composite as pacemaker kernel. Modulation into AB-PD and AB-PD & LP is most strongly correlated. AB-PD is responsive to modulatory input and drives the circuit rhythm.

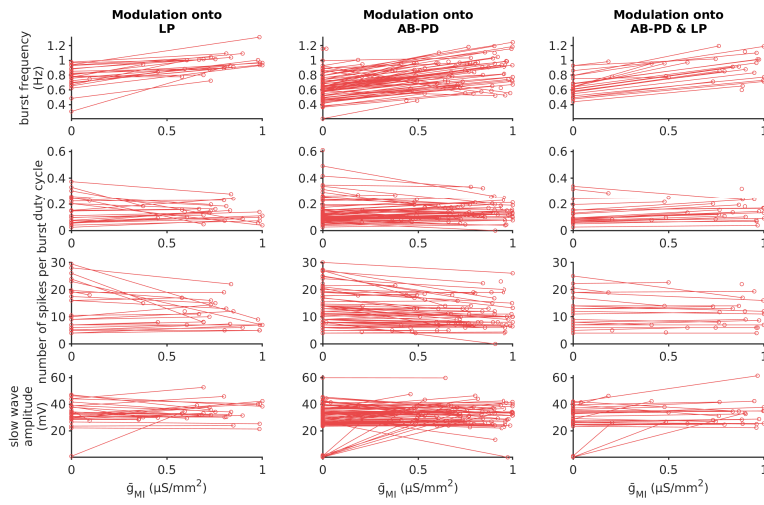


Figure 3.16: 146 network models in decentralized and modulated cases show increased burst frequency and amplitude under modulated conditions with respect to decentralization. Modulation under AB-PD and LP produces the most regular triphasic output. Colors indicate cells (red is LP).

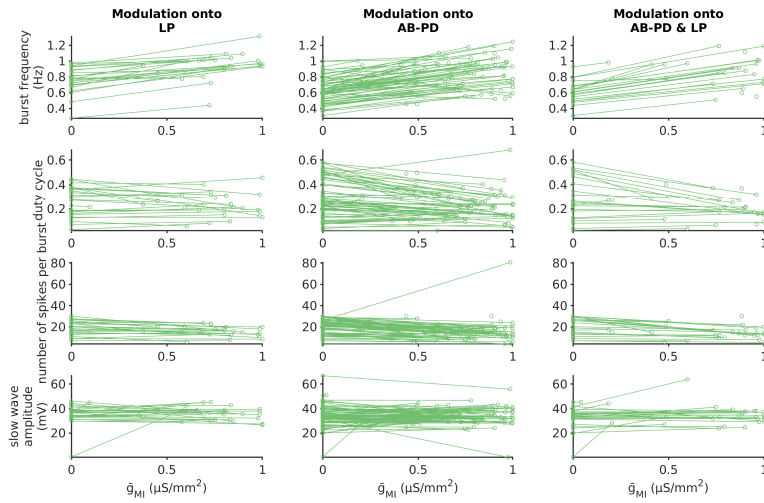


Figure 3.17: 146 network models in decentralized and modulated cases show increased burst frequency and amplitude under modulated conditions with respect to decentralization. Modulation under AB-PD and LP produces the most regular triphasic output. Colors indicate cells (green is PY).

3.2.3 Modulation of LP Can Inhibit AB-PD

[Figure 3.18](#) demonstrates a case where modulation onto [LP](#) decreases [AB-PD](#) burst frequency, but modulation onto the pacemaker or [AB-PD](#) and [LP](#) increases burst frequency. In [Figure 3.19](#), the slow-wave amplitude and frequency of [LP](#) increases, inhibiting the pacemaker, which bursts at a much slower frequency. If modulation is applied to [AB-PD](#) or the pacemaker kernel and [LP](#), the frequency increases. If the strength of the synapse is strong, pacemaker burst frequency decreases.

Applied current or I_{MI} tends to drive the rhythm, increasing burst frequency^{8,60}. Modulation onto [LP](#) inhibits the pacemaker, causing [AB-PD](#) to skip every other burst ([Figure 3.20](#)). In both [Figure 3.18](#) and [Figure 3.20](#), rhythmicity is maintained because synaptic transmission in the [STG](#) is partially graded. Instead, if modulation is applied to the pacemaker kernel or the pacemaker kernel and [LP](#), the frequency increases by 60% ([Figure 3.20](#)). These models recapitulate the role of [AB-PD](#) as the pacemaker kernel in the pyloric circuit.

Modulated neurons tend to maintain the same number of spikes per burst and duty cycle despite the higher frequency^{38,60}. Those which are not modulated typically fall behind. This is likely due to the fact that modulation acts at the spike threshold but does not contribute significantly to the spiking waveform. Non-modulated cells experience increased inhibition in the same period of time; the membrane potential does not depolarize as much between bouts of inhibition, decreasing slow-wave amplitude.

3.2.4 Modulation of AB Can Elicit Tonic Spiking

In some cases in the model, modulation onto the pacemaker has deleterious effects on the rhythm. If [AB-PD](#) is depolarized by addition of inward current near the spiking threshold, rhythmicity is lost ([Figure 3.22](#)); the neuron is close to a transition to a tonic spiking regime. If instead, [LP](#) is modulated, increasing inhibition onto the pacemaker drives the frequency ([Figure 3.23](#)). Interestingly, in the case where I_{MI} activates in the pacemaker kernel and [LP](#), rhythmicity is maintained, and burst frequency and slow-wave amplitude increase.

This result is likely non-physiological. Injected current into [AB](#) depolarizes the membrane, but generally does not elicit tonic spiking ([Figure 1.5](#))^{39,40}. The pacemaker is also not readily susceptible loss of rhythmicity from hyperpolarization due to a constant current⁴⁰. The modulatory input recorded in Swensen & Marder³⁹ cannot produce the sustained excitatory or inhibitory pulses of current necessary to cease endogenous bursting. In light of this, modulation onto [LP](#) contributes less to the increase in burst frequency and amplitude seen with proctolin and [RPCH](#).

Given that most AB-PD pacemakers must be far from transitions into depolarization block and tonic spiking regimes and be robust to hyperpolarization^{14,61}, the models suggest that modulation of LP likely serves an ancillary role in initiation and maintenance of robust triphasic motor patterns. These conclusions are supported by experiments with crustacean cardioactive peptide (CCAP), in which modulation of LP while the pacemaker was hyperpolarized was insufficient to initiate the pyloric rhythm⁶¹.

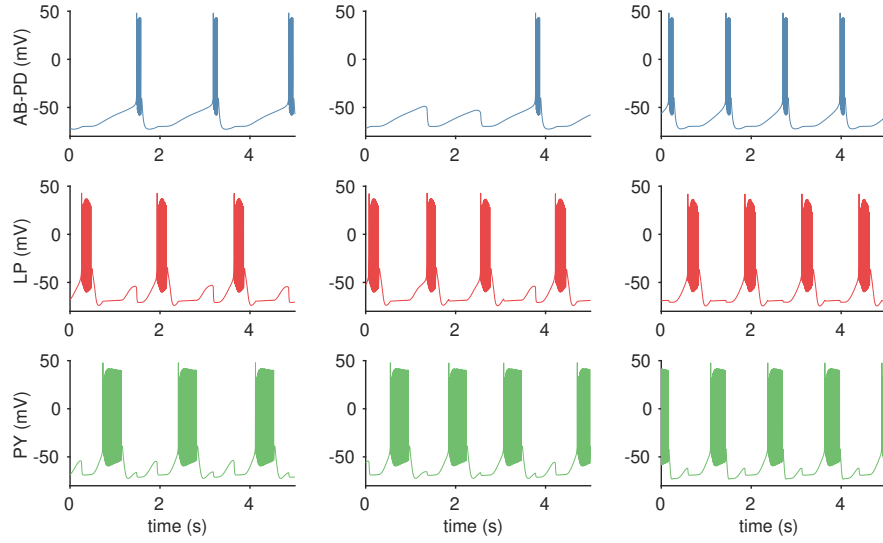


Figure 3.18: Neuromodulation onto LP can inhibit the pacemaker. Cells in columns are in the same network. *Left:* No neuromodulation and a normal triphasic rhythm. *Middle:* $\bar{g}_{MI}^{LP} = 0.2 \mu\text{S}/\text{mm}^2$, the pacemaker is inhibited by LP. *Right:* Recovery, where $\bar{g}_{MI}^{LP} = \bar{g}_{MI}^{AB-PD} = 0.6 \mu\text{S}/\text{mm}^2$, normal triphasic rhythm with increased frequency.

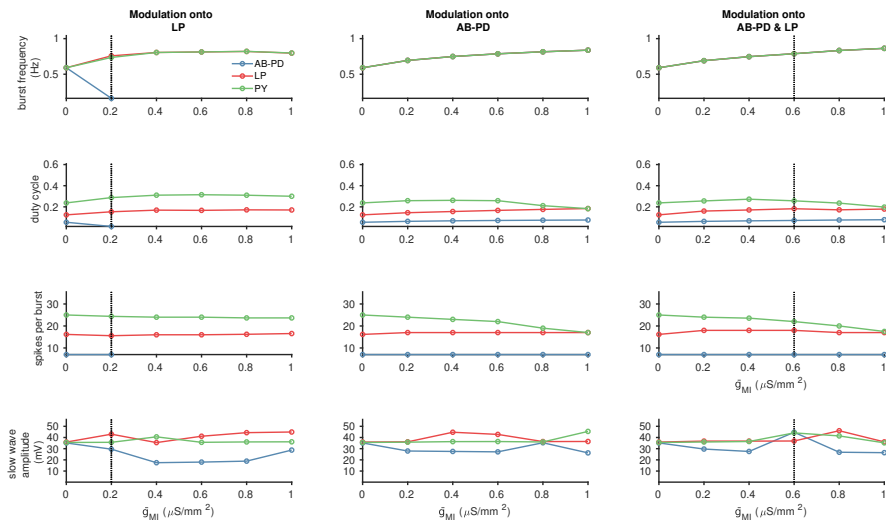


Figure 3.19: Neuromodulation onto LP can inhibit the pacemaker. Columns display metrics calculated at steady-state for three cases of modulation. Colors indicate cells (blue is AB-PD, red is LP, green is PY). Voltage traces at the dotted lines are shown in Figure 3.18.

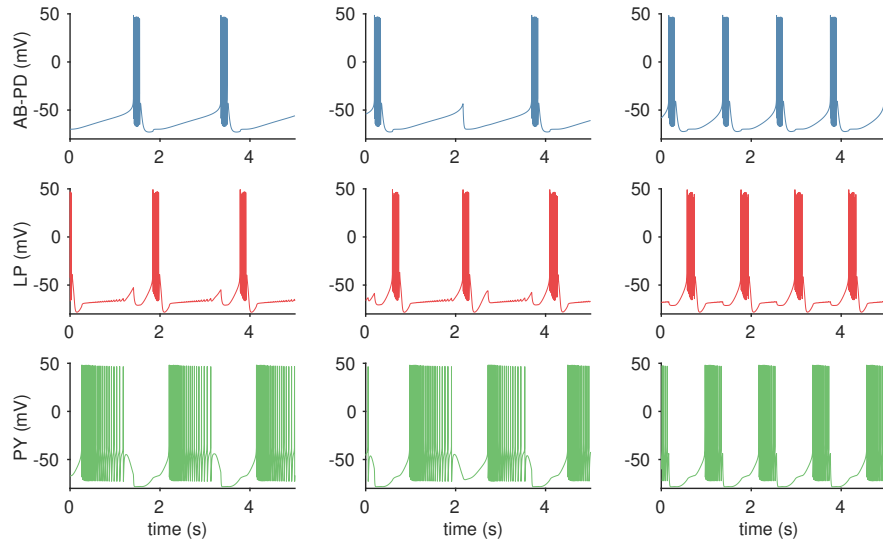


Figure 3.20: Neuromodulation onto LP does not increase burst frequency. Cells in columns are in the same network. *Left:* No neuromodulation and a normal triphasic rhythm. *Middle:* $\bar{g}_{MI}^{LP} = 0.8 \mu\text{S}/\text{mm}^2$, LP inhibits AB-PD. *Right:* Recovery, where $\bar{g}_{MI}^{LP} = \bar{g}_{MI}^{AB-PD} = 1.0 \mu\text{S}/\text{mm}^2$, normal triphasic rhythm with increased frequency.

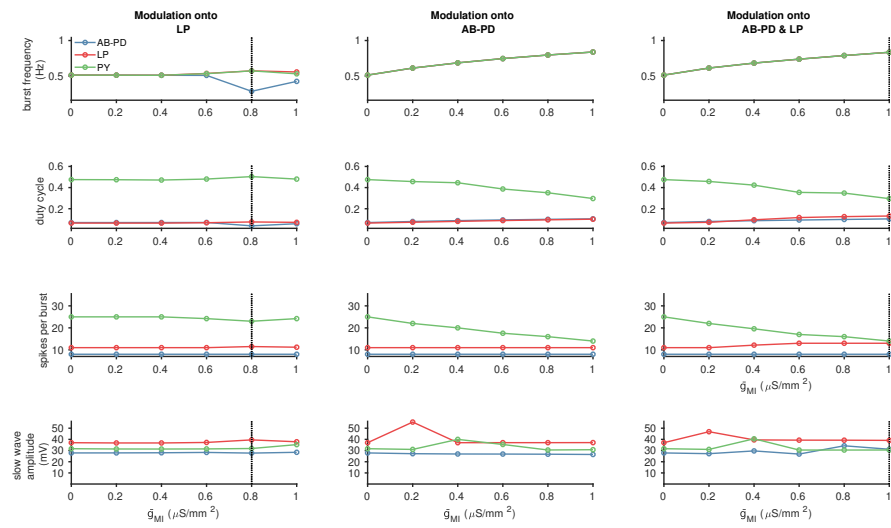


Figure 3.21: Neuromodulation onto LP does not increase burst frequency in many models. Columns display metrics calculated at steady-state for three cases of modulation. Colors indicate cells (blue is AB-PD, red is LP, green is PY). Voltage traces at the dotted lines are shown in Figure 3.20.

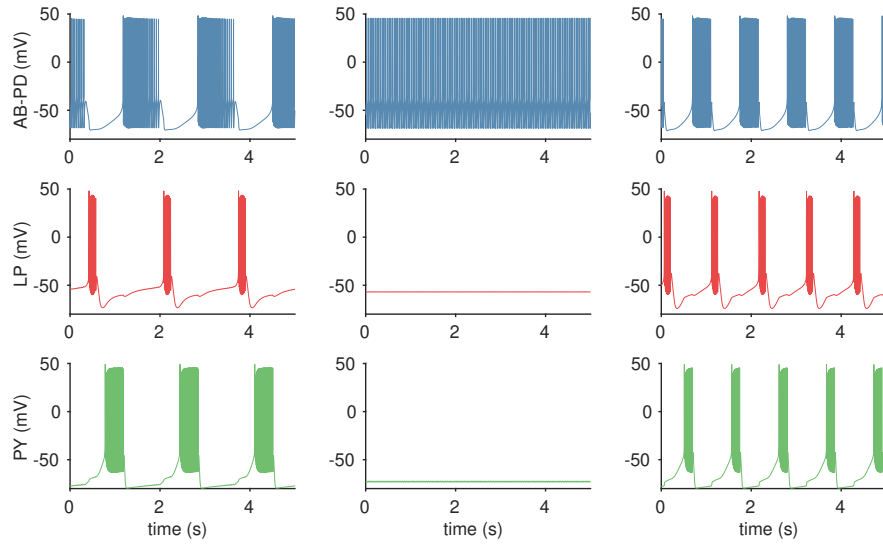


Figure 3.22: Neuromodulation onto AB-PD can depolarize AB-PD. Cells in columns are in the same network. *Left:* No neuromodulation and a normal triphasic rhythm. *Middle:* $\bar{g}_{MI}^{AB-PD} = 0.6 \mu\text{S}/\text{mm}^2$, AB-PD is tonically spiking. *Right:* Normal triphasic rhythm, where $\bar{g}_{MI}^{LP} = \bar{g}_{MI}^{AB-PD} = 1.0 \mu\text{S}/\text{mm}^2$, normal triphasic rhythm with increased frequency.

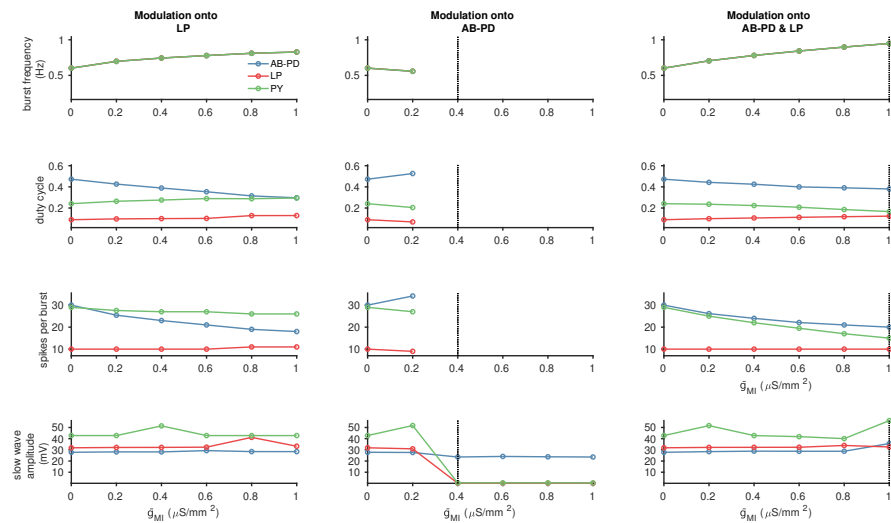


Figure 3.23: Modulation onto AB-PD can depolarize the pacemaker, resulting in tonic spiking. Modulation of LP or AB-PD and LP results in normal triphasic rhythm with increasing burst frequency. Voltage traces at the dotted lines are shown in Figure 3.22.

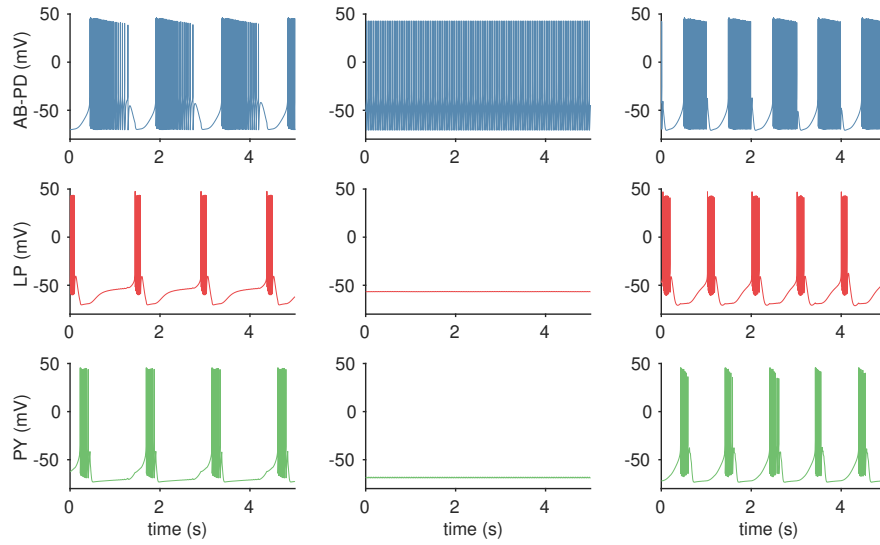


Figure 3.24: Neuromodulation of AB-PD can depolarize AB-PD. Cells in columns are in the same network. *Left:* No neuromodulation and a normal triphasic rhythm. *Middle:* $\bar{g}_{MI}^{AB-PD} = 0.6 \mu\text{S}/\text{mm}^2$, AB-PD is tonically spiking. *Right:* Normal triphasic rhythm, where $\bar{g}_{MI}^{LP} = \bar{g}_{MI}^{AB-PD} = 1.0 \mu\text{S}/\text{mm}^2$, normal triphasic rhythm with increased frequency.

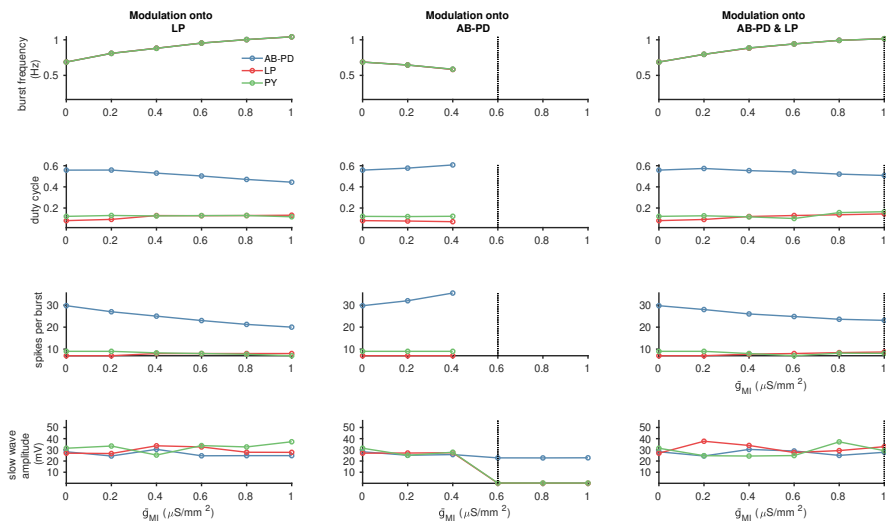


Figure 3.25: Neuromodulation of the pacemaker model can result in tonic spiking. Modulation of LP offsets this effect, resulting in triphasic activity with increased frequency and amplitude with respect to the decentralized condition.

4

CONCLUSION

Neuronal networks must produce stable circuit output for sustained periods of time despite environmental perturbation. In addition, they must be sensitive to key endogenous signaling to produce differing output. The **STG** manages these competing objectives while remaining degenerate to ion channel density. Neuromodulators can produce a diverse set of network states using the same cellular and synaptic morphology. In particular to the **STG**, the dense, tangled neuropil and gradations in reversal potential render neurons isopotential with respect to the somata. Neuromodulators, then, play the role of maintaining and switching network activity.

Many neuromodulators, such as proctolin and **RPCH** activate an inward mixed-cation I_{MI} . This current drives the network by activating near the spiking threshold. Networks with I_{MI} experience more stable, faster rhythms in comparison to decentralized states.

The **STG** database demonstrated cellular and network degeneracy with respect to maximal conductances, but did not incorporate the effects of modulation. Only a small subset of Prinz models respond to modulatory input (Figure A.1). Optimization by gradient descent produced a set of single-compartment **AB** models which increase in frequency slowly as a function of modulatory input maximal conductance (Figure A.3). Amplitude of these oscillations shifted from sub-threshold (< 20 mV) to high amplitude (> 20 mV) over a small range of modulatory input. Within these two regimes, the amplitude did not strongly depend on modulatory input. These data indicate that the models undergo amplitude transition with modulatory input switching the model between these qualitative states.

Using particle swarm optimization, models were simulated over a smaller range of I_{MI} maximal conductance (Figure 3.3). At low maximal conductance, **AB** models increase in frequency and amplitude as a smooth function of I_{MI} . Over larger ranges of maximal conductance, models converge to the sharp increase. These results recapitulate dose-responser curve data at low concentrations of oxotremorine (D. Hampton, unpublished) and **RPCH**³⁶.

Optimization of network models demonstrated I_{MI} in single compartment network models. While network models in this form have been shown to be degenerate with respect to ionic and synaptic maximal conductances^{46,47,50}, robustness to modulatory input has not been well studied. In basal conditions, network models received modulatory input into **AB-PD**, **LP**, or both. When modulatory input was removed, burst frequency and amplitude decreased (Figure 3.4), and

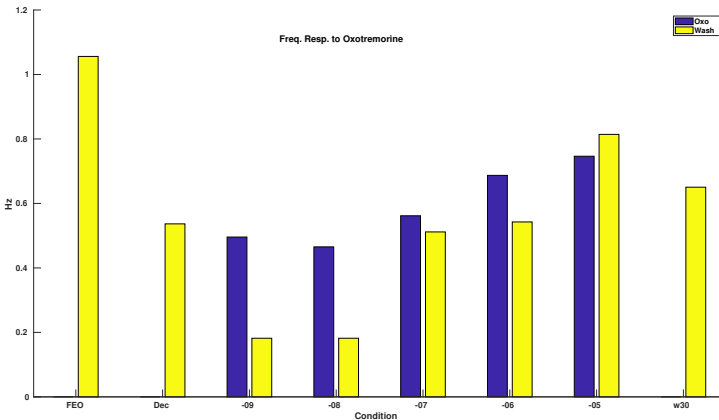


Figure 4.1: Burst frequency dose response to oxotremorine at low concentration demonstrates increasing response to modulatory input (D. Hampton, unpublished). Yellow bars indicate wash in physiological saline, blue indicates presence of oxotremorine in logarithmic molar concentration.

some models lost triphasic rhythmicity (Figure 3.8, Figure 3.6). These examples demonstrate the power of particle swarm optimization to produce models which fit arbitrary constraints. Single-compartment three-cell networks are capable of reproducing the neurocomputational effects of modulation on the pyloric rhythm.

When optimization protocols did not favor any particular modulation state (AB-PD, LP, or both), modulation into AB-PD and LP was revealed to be the most reliable method to initiate pyloric rhythmicity from a non-triphasic network, and increase burst frequency and slow wave amplitude in triphasic, decentralized networks (Figure 3.14). AB cells near transitions to tonic firing or depolarization block are uncommon *in-vitro*. Models near these points in parameter space tend to increase in burst frequency with I_{MI} in LP (Figure 3.22) and transition out of triphasic activity with modulation into AB-LP (Figure 3.24).

Of triphasic networks with pacemaker kernels robust to external depolarization and hyperpolarization, none showed increased burst frequency and amplitude during LP modulation with respect to the decentralized condition (Figure 3.14). These models display qualitatively similar activity to experimental results with CCAP⁶¹. Modulation onto LP provides antiphase hyperpolarization to PD. In conjunction with I_{MI} in AB-PD, RPCH and other neuromodulators drive robust pyloric rhythmicity.

Correlations between maximal conductances in cases where networks are non-pyloric in decentralized conditions and pyloric under neuromodulation against control conditions pyloric everywhere. Networks which became pyloric under neuromodulation tended to have lower calcium conductances (Figure 3.10). In addition, LP mod-

els tuned I_{KCa} to I_H . These relationships indicate strong potential for post-inhibitory rebound-mediated bursting. The results provide support for AB-PD as pacemaker that drives LP and PY. Modulation of PY is likely less necessary because of the many electrically coupled neurons and half-center connection to LP. PY can readily generate trains of action potentials down descending axons when inhibited rhythmically by AB, PD, and LP.

These investigations were motivated by P. Rosenbaum's experiments in TTX and RPCH which demonstrated stereotyped rhythmic oscillations unique to each preparation. Rhythmic activity with periods on the order of 5-10 s were observed. This timescale is vastly longer than intrinsic dynamics of any currents contributing to the change in membrane potential. Computational work endeavored to propose a hypothesis for these phenomena.

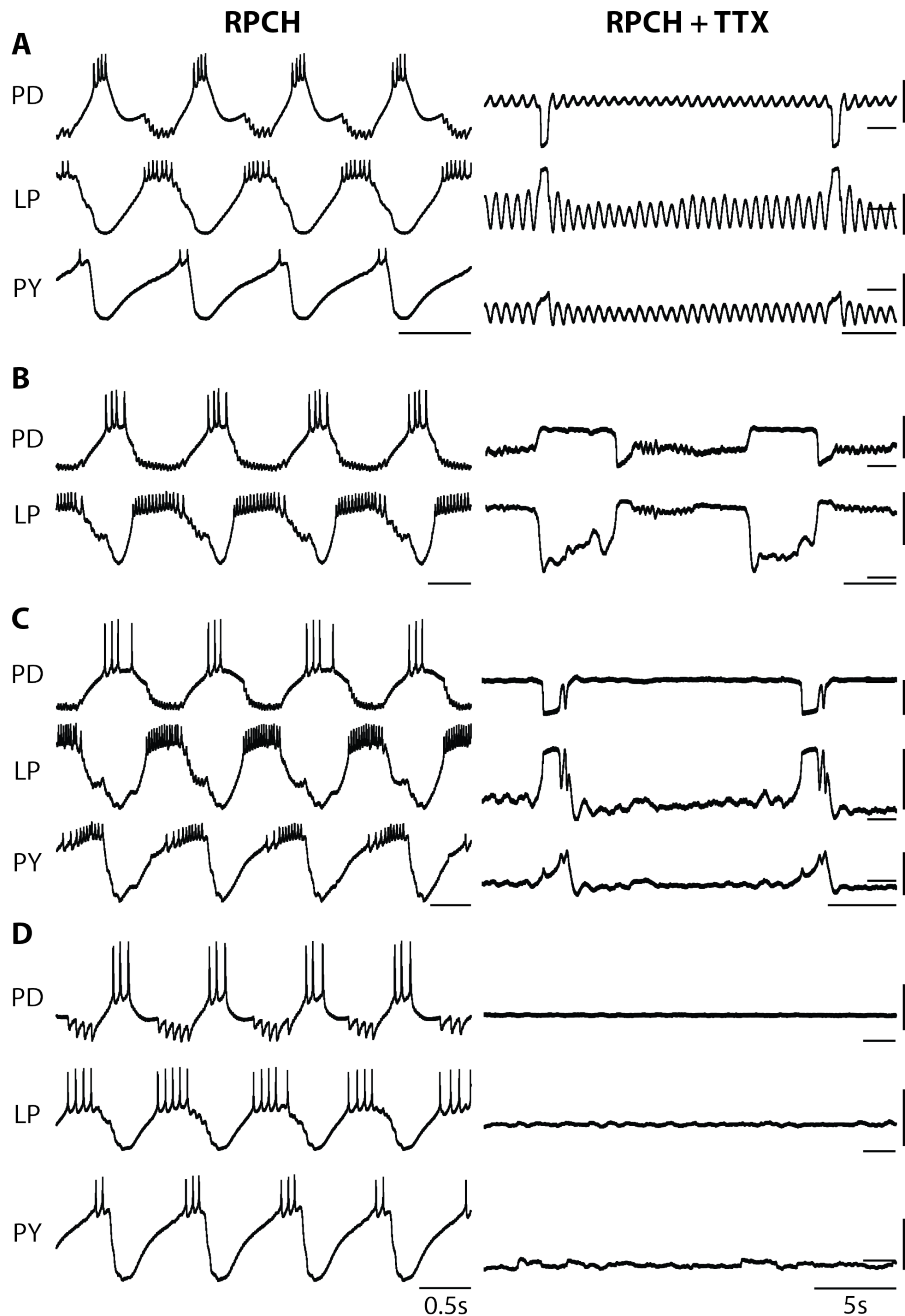


Figure 4.2: Start of RPCH-TTX rhythm. No rhythmic activity in TTX, but after application of RPCH rhythms start A, with large amplitude, slow frequency oscillations in both PD and LP predominantly large amplitude slow frequency oscillations. Vertical scale bars denote 10 mV, horizontal scale bars membrane potential at -50 mV (P. Rosenbaum, unpublished).

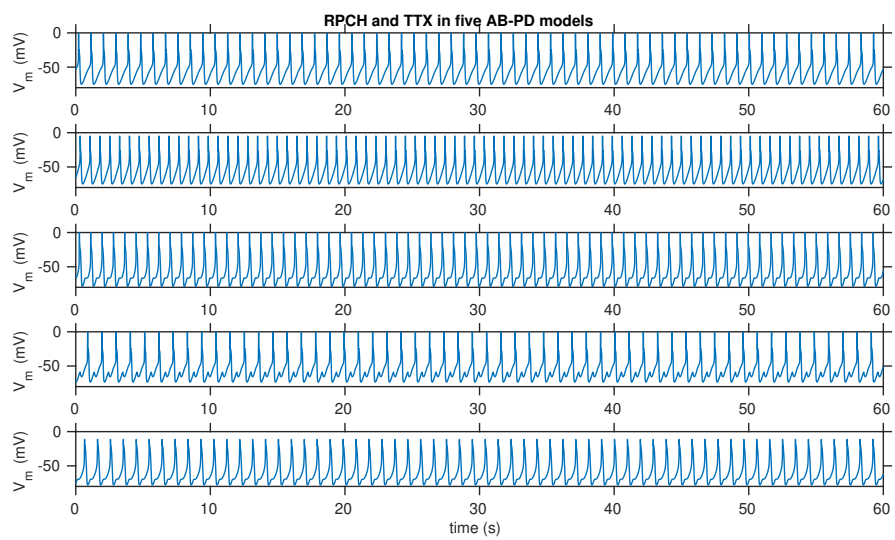


Figure 4.3: [RPCH](#) and [TTX](#) in [AB-PD](#) models produces rhythmic activity. Simulated data are asymptotically stable, without phenomena on timescales > 2 s. Graded synaptic transmission maintains triphasic rhythm in the absence of sodium spikes.

The three cell model does not, at this time, account for any effects on timescales > 2 s. When additional cells contributing to the pyloric network were added (viz. **IC**, **VD**), plateau potentials emerged in **LP** at timescales > 5 s. In order to develop a model that recapitulates the underlying variability revealed by **RPCH** and **TTX**, a more complete model of the pyloric circuit must be developed. In the current timescale, this thesis demonstrates that single-compartment three-cell network models of the pyloric rhythm are sufficiently complex to reproduce the effects of **IMI**. The models maintain the maximal conductance degeneracy of previous work, while demonstrating robustness to modulatory input. The simulation environment **xolotl** and particle swarm optimization protocols are ready to be implemented on larger scale endeavors.

A

APPENDIX

A.1 MAXIMAL CONDUCTANCES FOR MODEL NEURONS

The dynamics and compartment parameters of each model neuron are described in [Chapter 2](#). The maximal conductances are as follows

CURRENT	\bar{g} ($\mu\text{S}/\text{mm}^2$)	NOTES
I_A	1844	
I_{CaS}	103	
I_H	0.39	
I_{KCa}	214	
I_{Kd}	1746.96	
I_{MI}	1	0 in the decentralized case

Table A.1: Maximal conductances for [Figure 3.3](#).

CURRENT	AB-PD \bar{g} ($\mu\text{S}/\text{mm}^2$)	LP \bar{g} ($\mu\text{S}/\text{mm}^2$)	PY \bar{g} ($\mu\text{S}/\text{mm}^2$)
I_A	483.25	341.98	449.88
I_{CaS}	18.647	39.765	85.009
I_{CaT}	30.368	14.649	9.9027
I_H	0.14027	0.47477	0.3751
I_{KCa}	99.998	88.89	14.637
I_{Kd}	1030.1	1093	1228.2
I_{Na}	1274.5	985.64	1797.1

Table A.2: Maximal conductances for [Figure 3.4](#).

CURRENT	PRESYNAPTIC	POSTSYNAPTIC	\bar{g} ($\mu\text{S}/\text{mm}^2$)
I_{chol}	AB-PD	LP	59.724
I_{chol}	AB-PD	PY	94.508
I_{glut}	AB-PD	LP	79.803
I_{glut}	AB-PD	PY	97.881
I_{glut}	LP	PY	1.6985
I_{glut}	PY	LP	84.74
I_{glut}	LP	AB-PD	0.0128

Table A.3: Maximal conductances for Figure 3.4.

CURRENT	AB-PD \bar{g} ($\mu\text{S}/\text{mm}^2$)	LP \bar{g} ($\mu\text{S}/\text{mm}^2$)	PY \bar{g} ($\mu\text{S}/\text{mm}^2$)
I_A	499.57	488.85	150.95
I_{CaS}	42.16	5.9231	100
I_{CaT}	29.236	48.989	0.00081
I_H	0.3182	0.3666	0.1264
I_{KCa}	100	62.559	99.359
I_{Kd}	878.65	911.94	816.2
I_{Na}	990.11	1733.6	1926.2

Table A.4: Maximal conductances for Figure 3.6.

CURRENT	PRESYNAPTIC	POSTSYNAPTIC	\bar{g} ($\mu\text{S}/\text{mm}^2$)
I_{chol}	AB-PD	LP	43.589
I_{chol}	AB-PD	PY	91.146
I_{glut}	AB-PD	LP	46.6953
I_{glut}	AB-PD	PY	71.918
I_{glut}	LP	PY	7.2045
I_{glut}	PY	LP	4.0693
I_{glut}	LP	AB-PD	43.899

Table A.5: Maximal conductances for Figure 3.6.

CURRENT	AB-PD \bar{g} ($\mu\text{S}/\text{mm}^2$)	LP \bar{g} ($\mu\text{S}/\text{mm}^2$)	PY \bar{g} ($\mu\text{S}/\text{mm}^2$)
I_A	384.09	215.15	398.88
I_{CaS}	4.7276	21.739	91.294
I_{CaT}	40.901	55.179	4.7064
I_H	0.26391	0.48577	0.49937
I_{KCa}	56.614	83.753	6.9534
I_{Kd}	766.44	1196	1103.7
I_{Na}	1719.3	1791.4	1978.6

Table A.6: Maximal conductances for Figure 3.8.

CURRENT	PRESYNAPTIC	POSTSYNAPTIC	\bar{g} ($\mu\text{S}/\text{mm}^2$)
I_{chol}	AB-PD	LP	0.70694
I_{chol}	AB-PD	PY	2.5239
I_{glut}	AB-PD	LP	14.382
I_{glut}	AB-PD	PY	96.992
I_{glut}	LP	PY	22.72
I_{glut}	PY	LP	16.11
I_{glut}	LP	AB-PD	54.05

Table A.7: Maximal conductances for Figure 3.8.

CURRENT	AB-PD \bar{g} ($\mu\text{S}/\text{mm}^2$)	LP \bar{g} ($\mu\text{S}/\text{mm}^2$)	PY \bar{g} ($\mu\text{S}/\text{mm}^2$)
I_A	48.274	486.59	361.85
I_{CaS}	0.95921	52.628	35.453
I_{CaT}	44.247	31.541	58.985
I_H	0.057166	0.42321	0.42576
I_{KCa}	63.068	93.046	54
I_{Kd}	957.19	1075.4	1153.9
I_{Na}	1584.4	1196.8	1835.9

Table A.8: Maximal conductances for Figure 3.18.

CURRENT	PRESYNAPTIC	POSTSYNAPTIC	\bar{g} ($\mu\text{S}/\text{mm}^2$)
I_{chol}	AB-PD	LP	21.247
I_{chol}	AB-PD	PY	17.497
I_{glut}	AB-PD	LP	92.692
I_{glut}	AB-PD	PY	74.007
I_{glut}	LP	PY	97.419
I_{glut}	PY	LP	93.541
I_{glut}	LP	AB-PD	51.799

Table A.9: Maximal conductances for Figure 3.18.

CURRENT	AB-PD \bar{g} ($\mu\text{S}/\text{mm}^2$)	LP \bar{g} ($\mu\text{S}/\text{mm}^2$)	PY \bar{g} ($\mu\text{S}/\text{mm}^2$)
I_A	9.5645	0	67.751
I_{CaS}	6.8258	30.335	32.357
I_{CaT}	27.819	0.12634	5.7595
I_H	0.029794	0.38326	0.26788
I_{KCa}	82.919	85.903	49.91
I_{Kd}	1180.3	254.78	1188.6
I_{Na}	1934	1707.7	1895.7

Table A.10: Maximal conductances for Figure 3.20.

CURRENT	PRESYNAPTIC	POSTSYNAPTIC	\bar{g} ($\mu\text{S}/\text{mm}^2$)
I_{chol}	AB-PD	LP	18.975
I_{chol}	AB-PD	PY	100
I_{glut}	AB-PD	LP	15.721
I_{glut}	AB-PD	PY	19.862
I_{glut}	LP	PY	27.179
I_{glut}	PY	LP	63.191
I_{glut}	LP	AB-PD	59.59

Table A.11: Maximal conductances for Figure 3.20.

CURRENT	AB-PD \bar{g} ($\mu\text{S}/\text{mm}^2$)	LP \bar{g} ($\mu\text{S}/\text{mm}^2$)	PY \bar{g} ($\mu\text{S}/\text{mm}^2$)
I_A	142.64	280.07	20.373
I_{CaS}	53.39	31.45	14.268
I_{CaT}	7.0457	36.037	53.337
I_H	0.11766	0.49646	0.37665
I_{KCa}	87.08	84.953	20.246
I_{Kd}	782.28	718.61	1026.5
I_{Na}	1846	1702.4	1998.7

Table A.12: Maximal conductances for Figure 3.22.

CURRENT	PRESYNAPTIC	POSTSYNAPTIC	\bar{g} ($\mu\text{S}/\text{mm}^2$)
I_{chol}	AB-PD	LP	0.001
I_{chol}	AB-PD	PY	84.207
I_{glut}	AB-PD	LP	5.7983
I_{glut}	AB-PD	PY	1.6739
I_{glut}	LP	PY	95.435
I_{glut}	PY	LP	7.7081
I_{glut}	LP	AB-PD	97.889

Table A.13: Maximal conductances for Figure 3.22.

CURRENT	AB-PD \bar{g} ($\mu\text{S}/\text{mm}^2$)	LP \bar{g} ($\mu\text{S}/\text{mm}^2$)	PY \bar{g} ($\mu\text{S}/\text{mm}^2$)
I_A	103.45	464.2	458.17
I_{CaS}	62.458	28.521	64.549
I_{CaT}	3.2673	39.564	6.7024
I_H	0.41882	0.41944	0.39775
I_{KCa}	99.338	87.122	68.104
I_{Kd}	1242.4	1023	1245.5
I_{Na}	1343.2	1862.4	1693.5

Table A.14: Maximal conductances for Figure 3.24.

CURRENT	PRESYNAPTIC	POSTSYNAPTIC	\bar{g} ($\mu\text{S}/\text{mm}^2$)
I_{chol}	AB-PD	LP	0.019872
I_{chol}	AB-PD	PY	24.633
I_{glut}	AB-PD	LP	4.1505
I_{glut}	AB-PD	PY	60.444
I_{glut}	LP	PY	10.058
I_{glut}	PY	LP	69.451
I_{glut}	LP	AB-PD	65.046

Table A.15: Maximal conductances for [Figure 3.24](#).

A.2 SUPPLEMENTAL FIGURES

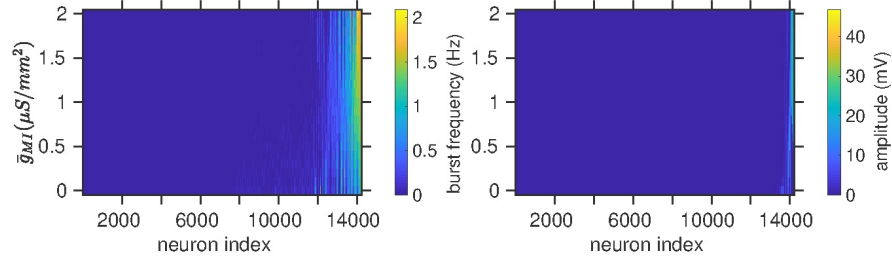


Figure A.1: Database models without I_{Na} or I_{CaT} with modulatory input respond over a small range of maximal conductance. Most database models do not respond to modulatory input. A subset increase in frequency and amplitude (peak voltage - trough voltage). Models are sorted by mean metric value.

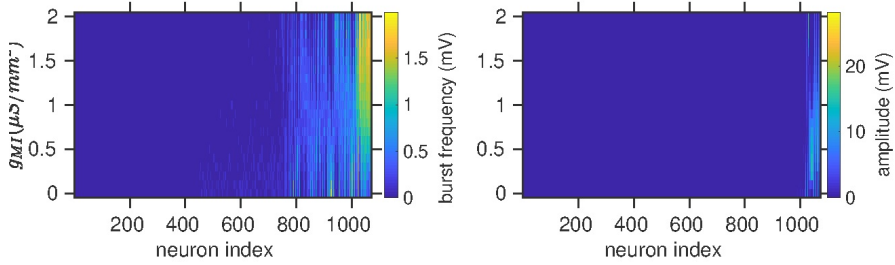


Figure A.2: A subset of database models with I_{Na} or I_{CaT} were responsive to modulatory input. The 1000 models with the greatest change in frequency and amplitude were plotted with updated color scaling. Models are sorted by mean metric value.

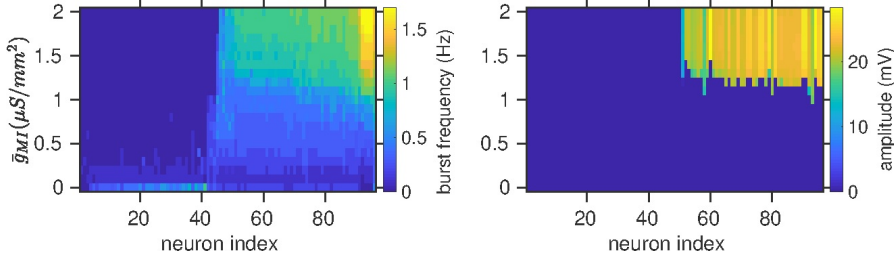


Figure A.3: Models optimized for a graded increase in frequency and amplitude under increasing modulatory input experience frequency as a graded transition and amplitude as a switch between quiescence and high amplitude. Optimized models display graded increase in burst frequency as the maximal conductance of modulatory input increases. Amplitude increases sharply during a transitional state as maximal conductance of I_{MI} increases. Models are sorted by mean metric value.

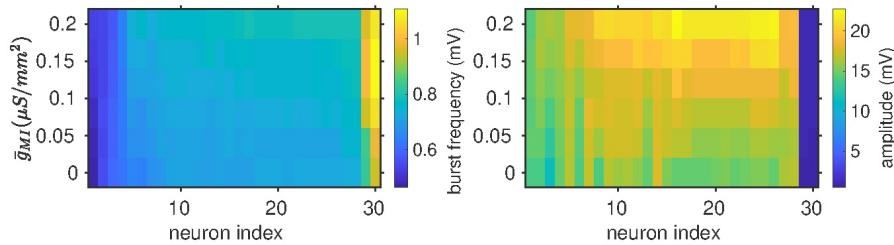


Figure A.4: Models optimized for a graded increase in burst frequency and amplitude over increasing modulatory input. Modulatory input increases the amplitude of slow-wave oscillations by increasing the peak voltage. In these models, the duty cycle remains constant and the frequency increases.

BIBLIOGRAPHY

1. Marder, E. & Bucher, D. Central Pattern Generators and the Control of Rhythmic Movements. *Current Biology* **11**, R986–R996. ISSN: 0960-9822 (Nov. 27, 2001) (cit. on pp. [1](#), [2](#), [4](#)).
2. Doi, A. & Ramirez, J.-M. Neuromodulation and the Orchestration of the Respiratory Rhythm. *Respiratory physiology & neurobiology* **164**, 96–104. ISSN: 1569-9048 (Dec. 10, 2008) (cit. on p. [1](#)).
3. Peña, F. & Ramirez, J.-M. Endogenous Activation of Serotonin-2A Receptors Is Required for Respiratory Rhythm Generation In Vitro. *Journal of Neuroscience* **22**, 11055–11064. ISSN: 0270-6474, 1529-2401 (Dec. 15, 2002) (cit. on p. [1](#)).
4. Nusbaum, M. P. *et al.* The Roles of Co-Transmission in Neural Network Modulation. *Trends in Neurosciences* **24**, 146–154. ISSN: 0166-2236 (Mar. 2001) (cit. on pp. [1](#), [4](#)).
5. Tononi, G., Sporns, O. & Edelman, G. M. Measures of Degeneracy and Redundancy in Biological Networks. *Proceedings of the National Academy of Sciences* **96**, 3257–3262. ISSN: 0027-8424, 1091-6490 (1999) (cit. on p. [1](#)).
6. Edelman, G. M. & Gally, J. A. Degeneracy and Complexity in Biological Systems. *Proceedings of the National Academy of Sciences* **98**, 13763–13768. ISSN: 0027-8424, 1091-6490 (Nov. 20, 2001) (cit. on p. [1](#)).
7. Whitacre, J. & Bender, A. Degeneracy: A Design Principle for Achieving Robustness and Evolvability. *Journal of Theoretical Biology* **263**, 143–153. ISSN: 0022-5193 (Mar. 7, 2010) (cit. on p. [1](#)).
8. Drion, G., O’Leary, T. & Marder, E. Ion Channel Degeneracy Enables Robust and Tunable Neuronal Firing Rates. *Proceedings of the National Academy of Sciences* **112**, E5361–E5370. ISSN: 0027-8424, 1091-6490 (Sept. 22, 2015) (cit. on pp. [1](#), [36](#)).
9. Marder, E. & Calabrese, R. L. Principles of Rhythmic Motor Pattern Generation. *Physiological Reviews* **76**, 687–717. ISSN: 0031-9333 (July 1996) (cit. on p. [1](#)).
10. Maynard, D. M. Simpler Networks. *Annals of the New York Academy of Sciences* **193**, 59–72. ISSN: 0077-8923 (Aug. 25, 1972) (cit. on p. [1](#)).
11. Hartline, D. K. Pattern Generation in the Lobster (*Panulirus*) Stomatogastric Ganglion. *Biological Cybernetics* **33**, 223–236. ISSN: 0340-1200, 1432-0770 (Aug. 1, 1979) (cit. on p. [1](#)).

12. Raper, J. A. Nonimpulse-Mediated Synaptic Transmission during the Generation of a Cyclic Motor Program. *Science (New York, N.Y.)* **205**, 304–306. ISSN: 0036-8075 (July 20, 1979) (cit. on p. 1).
13. *The Crustacean Stomatogastric System* (eds Selverston, A. & Moulins, M.) (1987). ISBN: 978-3-642-71516-7. <http://www.springer.com/us/book/9783642715181> (2017) (cit. on pp. 1, 3).
14. Harris-Warrick, R. M. et al. *Dynamic Biological Networks: The Stomatogastric Nervous System* 366 pp. ISBN: 978-0-262-08214-3 (MIT Press, 1992) (cit. on pp. 1, 3, 37).
15. Marder, E., Goeritz, M. L. & Otopalik, A. G. Robust Circuit Rhythms in Small Circuits Arise from Variable Circuit Components and Mechanisms. *Current Opinion in Neurobiology. SI: Brain rhythms and dynamic coordination* **31**, 156–163. ISSN: 0959-4388 (Apr. 1, 2015) (cit. on p. 2).
16. Marder, E. Neuromodulation of Neuronal Circuits: Back to the Future. *Neuron* **76**, 1–11. ISSN: 0896-6273 (Oct. 4, 2012) (cit. on pp. 2, 4).
17. Nusbaum, Michael P., Blitz, Dawn M. & Marder, Eve. Functional Consequences of Neuropeptide and Small-Molecule Co-Transmission. *Nature Reviews Neuroscience* **18**, 389–403. ISSN: 1471-003X (2017) (cit. on pp. 2–4).
18. Otopalik, A. G. et al. Sloppy Morphological Tuning in Identified Neurons of the Crustacean Stomatogastric Ganglion. *eLife* **6**, e22352. ISSN: 2050-084X (Feb. 8, 2017) (cit. on pp. 2, 7).
19. Cuntz, H. et al. One Rule to Grow Them All: A General Theory of Neuronal Branching and Its Practical Application. *PLoS computational biology* **6**. ISSN: 1553-7358. doi:[10.1371/journal.pcbi.1000877](https://doi.org/10.1371/journal.pcbi.1000877). pmid: [20700495](https://pubmed.ncbi.nlm.nih.gov/20700495/) (Aug. 5, 2010) (cit. on pp. 2, 7).
20. Hamood, A. W. & Marder, E. Consequences of Acute and Long-Term Removal of Neuromodulatory Input on the Episodic Gastric Rhythm of the Crab Cancer Borealis. *Journal of Neurophysiology* **114**, 1677–1692. ISSN: 0022-3077 (Sept. 2015) (cit. on pp. 2, 4, 20).
21. Hamood, A. W. et al. Quantitative Reevaluation of the Effects of Short- and Long-Term Removal of Descending Modulatory Inputs on the Pyloric Rhythm of the Crab, Cancer Borealis. *eNeuro* **2**, ENEURO.0058–14.2015. ISSN: 2373-2822 (Jan. 1, 2015) (cit. on p. 2).
22. Goldman, M. S. et al. Global Structure, Robustness, and Modulation of Neuronal Models. *Journal of Neuroscience* **21**, 5229–5238. ISSN: 0270-6474, 1529-2401 (July 15, 2001) (cit. on pp. 2, 4, 10).
23. Haddad, S. A. & Marder, E. Circuit Robustness to Temperature Perturbation Is Altered by Neuromodulators. *bioRxiv*, 178764 (Aug. 21, 2017) (cit. on pp. 2, 4).

24. Clemens, S. *et al.* Long-Term Expression of Two Interacting Motor Pattern-Generating Networks in the Stomatogastric System of Freely Behaving Lobster. *Journal of Neurophysiology* **79**, 1396–1408. ISSN: 0022-3077 (Mar. 1998) (cit. on p. 3).
25. Rezer, E. & Moulins, M. Expression of the Crustacean Pyloric Pattern Generator in the Intact Animal. *Journal of comparative physiology* **153**, 17–28. ISSN: 0340-7594, 1432-1351 (Mar. 1, 1983) (cit. on p. 3).
26. Marder, E. & Bucher, D. Understanding Circuit Dynamics Using the Stomatogastric Nervous System of Lobsters and Crabs. *Annual Review of Physiology* **69**, 291–316 (2007) (cit. on pp. 3, 18).
27. Hooper, S. L. & Marder, E. Modulation of the Lobster Pyloric Rhythm by the Peptide Proctolin. *The Journal of Neuroscience: The Official Journal of the Society for Neuroscience* **7**, 2097–2112. ISSN: 0270-6474 (July 1987) (cit. on p. 3).
28. Tang, L. S. *et al.* Robustness of a Rhythmic Circuit to Short- and Long-Term Temperature Changes. *The Journal of Neuroscience: The Official Journal of the Society for Neuroscience* **32**, 10075–10085. ISSN: 1529-2401 (July 18, 2012) (cit. on p. 4).
29. Johnson, B. R. & Harris-Warrick, R. M. Amine Modulation of Glutamate Responses from Pyloric Motor Neurons in Lobster Stomatogastric Ganglion. *Journal of Neurophysiology* **78**, 3210–3221. ISSN: 0022-3077 (Dec. 1997) (cit. on p. 4).
30. Nusbaum, M. P. & Beenhakker, M. P. A Small-Systems Approach to Motor Pattern Generation. *Nature* **417**, 417343a. ISSN: 1476-4687 (May 16, 2002) (cit. on p. 4).
31. Blitz, D. M. *et al.* Different Proctolin Neurons Elicit Distinct Motor Patterns from a Multifunctional Neuronal Network. *Journal of Neuroscience* **19**, 5449–5463. ISSN: 0270-6474, 1529-2401 (July 1, 1999) (cit. on p. 4).
32. Golowasch, J. & Marder, E. Ionic Currents of the Lateral Pyloric Neuron of the Stomatogastric Ganglion of the Crab. *Journal of Neurophysiology* **67**, 318–331. ISSN: 0022-3077 (Feb. 1992) (cit. on p. 4).
33. Golowasch, J. & Marder, E. Proctolin Activates an Inward Current Whose Voltage Dependence Is Modified by Extracellular Ca²⁺. *The Journal of Neuroscience: The Official Journal of the Society for Neuroscience* **12**, 810–817. ISSN: 0270-6474 (Mar. 1992) (cit. on pp. 4, 20).
34. Schulz, D. J., Goaillard, J.-M. & Marder, E. Variable Channel Expression in Identified Single and Electrically Coupled Neurons in Different Animals. *Nature Neuroscience* **9**, 356–362. ISSN: 1097-6256 (Mar. 2006) (cit. on pp. 4, 8).

35. O'Leary, T. *et al.* Correlations in Ion Channel Expression Emerge from Homeostatic Tuning Rules. *Proceedings of the National Academy of Sciences* **110**, E2645–E2654. ISSN: 0027-8424, 1091-6490 (July 9, 2013) (cit. on p. 4).
36. Nusbaum, M. P. & Marder, E. A Neuronal Role For a Crustacean Red Pigment Concentrating Hormone-Like Peptide: Neuromodulation of the Pyloric Rhythm in the Crab, Cancer Borealis. *Journal of Experimental Biology* **135**, 165–181. ISSN: 0022-0949, 1477-9145 (Mar. 1, 1988) (cit. on pp. 5, 20, 21, 23, 42).
37. Sharp, A. A. *et al.* Dynamic Clamp: Computer-Generated Conductances in Real Neurons. *Journal of Neurophysiology* **69**, 992–995. ISSN: 0022-3077, 1522-1598 (Mar. 1, 1993) (cit. on pp. 5, 20).
38. Swensen, A. M. & Marder, E. Multiple Peptides Converge to Activate the Same Voltage-Dependent Current in a Central Pattern-Generating Circuit. *The Journal of Neuroscience: The Official Journal of the Society for Neuroscience* **20**, 6752–6759. ISSN: 0270-6474 (Sept. 15, 2000) (cit. on pp. 5, 20, 36).
39. Swensen, A. M. & Marder, E. Modulators with Convergent Cellular Actions Elicit Distinct Circuit Outputs. *The Journal of Neuroscience: The Official Journal of the Society for Neuroscience* **21**, 4050–4058. ISSN: 1529-2401 (June 1, 2001) (cit. on pp. 5, 14, 20, 36).
40. Soto-Treviño, C. *et al.* Computational Model of Electrically Coupled, Intrinsically Distinct Pacemaker Neurons. *Journal of Neurophysiology* **94**, 590–604. ISSN: 0022-3077 (July 2005) (cit. on pp. 5, 8, 22, 36).
41. Abbott, L. F. & LeMasson, G. Analysis of Neuron Models with Dynamically Regulated Conductances. *Neural Computation* **5**, 823–842. ISSN: 0899-7667 (Nov. 1, 1993) (cit. on pp. 6, 8).
42. Liu, Z. *et al.* A Model Neuron with Activity-Dependent Conductances Regulated by Multiple Calcium Sensors. *The Journal of Neuroscience: The Official Journal of the Society for Neuroscience* **18**, 2309–2320. ISSN: 0270-6474 (1998) (cit. on pp. 6, 7, 9, 10).
43. Hodgkin, A. L. & Huxley, A. F. The Components of Membrane Conductance in the Giant Axon of Loligo. *The Journal of Physiology* **116**, 473–496. ISSN: 0022-3751 (Apr. 1952) (cit. on pp. 6, 9, 20).
44. Turrigiano, G., LeMasson, G. & Marder, E. Selective Regulation of Current Densities Underlies Spontaneous Changes in the Activity of Cultured Neurons. *The Journal of Neuroscience: The Official Journal of the Society for Neuroscience* **15**, 3640–3652. ISSN: 0270-6474 (5 Pt 1 May 1995) (cit. on pp. 6, 7, 9, 22).
45. Dayan, P. & Abbott, L. F. *Theoretical Neuroscience* xv+460. ISBN: 978-0-262-04199-7 (Massachusetts Institute of Technology Press, Cambridge, Mass., 2001) (cit. on pp. 7, 11).

46. Prinz, A. A., Billimoria, C. P. & Marder, E. Alternative to Hand-Tuning Conductance-Based Models: Construction and Analysis of Databases of Model Neurons. *Journal of Neurophysiology* **90**, 3998–4015. ISSN: 0022-3077 (Dec. 2003) (cit. on pp. 7–10, 20, 21, 42).
47. Prinz, A. A., Bucher, D. & Marder, E. Similar Network Activity from Disparate Circuit Parameters. *Nature Neuroscience* **7**, 1345–1352. ISSN: 1097-6256 (Dec. 2004) (cit. on pp. 7–9, 12, 20, 42).
48. O’Leary, T. et al. Cell Types, Network Homeostasis, and Pathological Compensation from a Biologically Plausible Ion Channel Expression Model. *Neuron* **82**, 809–821. ISSN: 0896-6273 (May 21, 2014) (cit. on p. 7).
49. Strogatz, S. *Sync: The Emerging Science of Spontaneous Order* 366 pp. ISBN: 978-0-7868-6844-5 (Hyperion Books, 2003) (cit. on p. 7).
50. Prinz, A. A. Computational Approaches to Neuronal Network Analysis. *Philosophical Transactions of the Royal Society B: Biological Sciences* **365**, 2397–2405. ISSN: 0962-8436 (Aug. 12, 2010) (cit. on pp. 8, 42).
51. Goaillard, J.-M. et al. Functional Consequences of Animal-to-Animal Variation in Circuit Parameters. *Nature Neuroscience* **12**, nn.2404. ISSN: 1546-1726 (Oct. 18, 2009) (cit. on p. 8).
52. Hamood, A. W. & Marder, E. Animal-to-Animal Variability in Neuromodulation and Circuit Function. *Cold Spring Harbor symposia on quantitative biology* **79**, 21–28. ISSN: 0091-7451 (2014) (cit. on pp. 8, 20).
53. Hodgkin, A. L., Huxley, A. F. & Katz, B. Measurement of Current-Voltage Relations in the Membrane of the Giant Axon of Loligo. *The Journal of Physiology* **116**, 424–448. ISSN: 0022-3751 (Apr. 28, 1952) (cit. on pp. 9, 20).
54. Hodgkin, A. L. & Huxley, A. F. A Quantitative Description of Membrane Current and Its Application to Conduction and Excitation in Nerve. *The Journal of Physiology* **117**, 500–544. ISSN: 0022-3751 (Aug. 28, 1952) (cit. on pp. 9, 10, 20).
55. Soofi, W. et al. Phase Maintenance in a Rhythmic Motor Pattern during Temperature Changes in Vivo. *Journal of Neurophysiology* **111**, 2603–2613. ISSN: 0022-3077 (June 15, 2014) (cit. on p. 9).
56. Freschi, J. E. Proctolin Activates a Slow, Voltage-Dependent Sodium Current in Motoneurons of the Lobster Cardiac Ganglion. *Neuroscience Letters* **106**, 105–111. ISSN: 0304-3940 (Nov. 20, 1989) (cit. on p. 10).
57. Abbott, L. et al. in *Methods in Neuronal Modeling: From Ions to Networks* 461–410 (MIT Press, Cambridge, Mass, 1998) (cit. on p. 10).

58. Savitzky, A. & Golay, M. J. E. Smoothing and Differentiation of Data by Simplified Least Squares Procedures. *Analytical Chemistry* **36**, 1627–1639. ISSN: 0003-2700 (July 1, 1964) (cit. on p. 19).
59. Peacock, J. A. Two-Dimensional Goodness-of-Fit Testing in Astronomy. *Monthly Notices of the Royal Astronomical Society* **202**, 615–627. ISSN: 0035-8711 (Mar. 1, 1983) (cit. on p. 33).
60. Eisen, J. S. & Marder, E. Mechanisms Underlying Pattern Generation in Lobster Stomatogastric Ganglion as Determined by Selective Inactivation of Identified Neurons. III. Synaptic Connections of Electrically Coupled Pyloric Neurons. *Journal of Neurophysiology* **48**, 1392–1415. ISSN: 0022-3077 (Dec. 1982) (cit. on p. 36).
61. Weimann, J. *et al.* Modulation of Oscillator Interactions in the Crab Stomatogastric Ganglion by Crustacean Cardioactive Peptide. *The Journal of neuroscience : the official journal of the Society for Neuroscience* **17**, 1748–60 (Apr. 1, 1997) (cit. on pp. 37, 43).

DECLARATION

I hereby certify that this thesis is entirely my own work. All code can be found at <https://gitlab.com/marderlab>.

Waltham, Massachusetts, May 2018

Alec J Hoyland

COLOPHON

This document was typeset using the typographical look-and-feel `classicthesis` developed by André Miede and Ivo Pletikosić. The style was inspired by Robert Bringhurst's seminal book on typography "*The Elements of Typographic Style*".